Cross Section Measurements for Quasielastic Neutron-Induced Deuteron Breakup

By

Katrina Koehler

A thesis submitted in partial fulfillment of the requirements
for the degree of

Bachelor of Science

Houghton College

May 2011

Signature of Author . . . . . .
Department of Physics
May14, 2011

. . . . . .
Dr. Mark Yuly
Professor of Physics
Research Supervisor

. . . . . .
Dr. Christopher Wells
Assistant Professor of Physics

Cross Section Measurements for Quasielastic Neutron-Induced Deuteron Breakup

By
Katrina Koehler
Submitted to the Houghton College Department of Physics
on May14, 2011
in partial fulfillment of the requirement for
the degree of Bachelor of Science

Abstract

An experiment to measure the quasielastic $d(n,np)n$ scattering cross sections at intermediate incident neutron energies, ranging up to 800 MeV, was conducted by a collaboration of researchers from Houghton College, MIT, the University of Kentucky and Los Alamos National Laboratory at the Los Alamos Neutron Science Center (LANSCE). Protons from deuteron breakup reaction travel through a magnetic spectrometer, consisting of an initial thin plastic DE scintillator, a set of drift chambers, two permanent magnets, another set of drift chambers and two rear plastic scintillators. An array of nine two-meter high plastic scintillators detects scattered neutrons. The np elastic scattering data collected in tandem with this experiment will be used to determine the normalization for the $n-d$ breakup cross section.

Thesis Supervisor: Dr. Mark Yuly
Title: Professor of Physics

TABLE OF CONTENTS

LIST OF FIGURES

LIST OF TABLES

Chapter 1

INTRODUCTION

1.1 The d(n,np)n Reaction

In 2009, a scattering experiment was conducted at the Los Alamos Neutron Science Center (LANSCE) in Los Alamos, New Mexico with collaborators from Massachusetts Institute of Technology (MIT), University of Kentucky, Los Alamos National Laboratory (LANL), and Boğaziçi University to find the scattering cross section for neutron-induced deuteron breakup, $d(n,np)n$. An incident neutron beam was used to break apart deuterons at quasielastic kinematics. In quasielastic scattering, the incident neutron interacts primarily with the proton, breaking up the deuterium nucleus, or deuteron, as seen in Figure 1.1. This is quasielastic because the other nucleon does not receive much transferred momentum, so the proton is deflected at roughly a conjugate angle for elastic scattering to the scattered neutron. However, the angle and energy spectra are broadened because the neutron and proton in the nucleus do have some momentum and some energy is transferred to the spectator neutron.

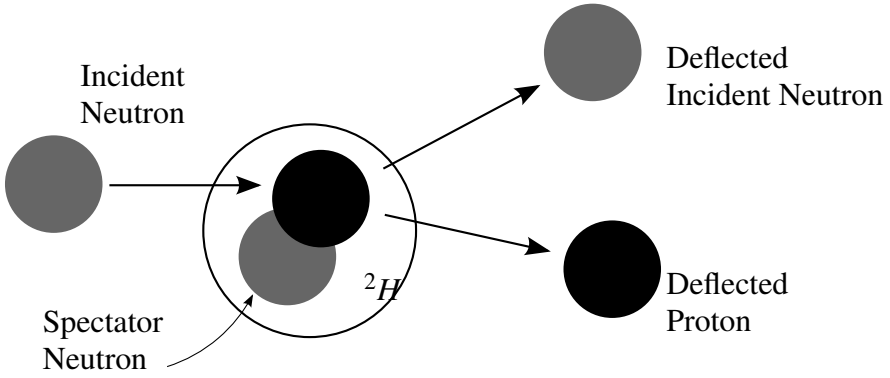

Figure 1.1 Schematic of quasielastic $n-d$ breakup. The neutron is incident on a deuterium nucleus, containing a proton (black) and a neutron (grey). In a quasi-free elastic scattering reaction, the incident neutron scatters from the proton, leaving the spectator neutron largely unaffected.

The experimental setup shown in Figure 1.2 was used to determine the energy and angle of the scattered neutron and proton, with the magnetic spectrometer to the right of the beam line

detecting scattered protons and the detector array on the left of the beam line detecting scattered neutrons. The incident neutron energy was determined using time of flight. An elastic monitor, consisting of a ΔE scintillator and Cesium Iodide detector located left of the beam were used to detect elastic neutron-deuteron scattering for normalization. A fission chamber located upstream of the deuterium target was used to obtain the number of incident neutrons. The neutron bar detector array located on beam left allowed multiple neutron deflection angles to be measured simultaneously. The deflected neutrons were detected in any one of nine vertical bars, determining nine angles. The magnetic spectrometer on beam right allowed even higher angular resolution for outgoing protons, by using the wire drift chamber tracking. The flight times for the scattered protons were used to calculate their energies, since the magnetic spectrometer did not work as well as expected. The energy of the protons allowed the time of flight (TOF) of the incident neutron to be determined, leading to the incident neutron energy.

1.2 Cross Sections

This experiment sought to measure the $d(n,np)n$ scattering cross section. The concept of cross section arises from the measured experimental quantities in a scattering experiment. Related to the probability that a reaction will take place, the cross section is independent of the details of the experimental setup, making it a useful quantity that can be easily compared between different experiments and used to test theoretical predictions.

As seen in Figure 1.3, for a thin target, the number of detected particles (dN_d) in a scattering experiment is proportional to the incident particles (N_{inc}), the number of scattering centers (N_t), and the detector solid angle ($d\Omega$), such that:

$$dN_d = \sigma(\theta) N_{inc} N_t d\Omega, \tag{1.1}$$

where $\sigma(\theta)$ is the proportionality constant called the cross section which is dependent on the scattering angle θ. The differential detector solid angle, measured in steradians (sr), is defined as:

$$d\Omega = \frac{dA}{r^2}, \tag{1.2}$$

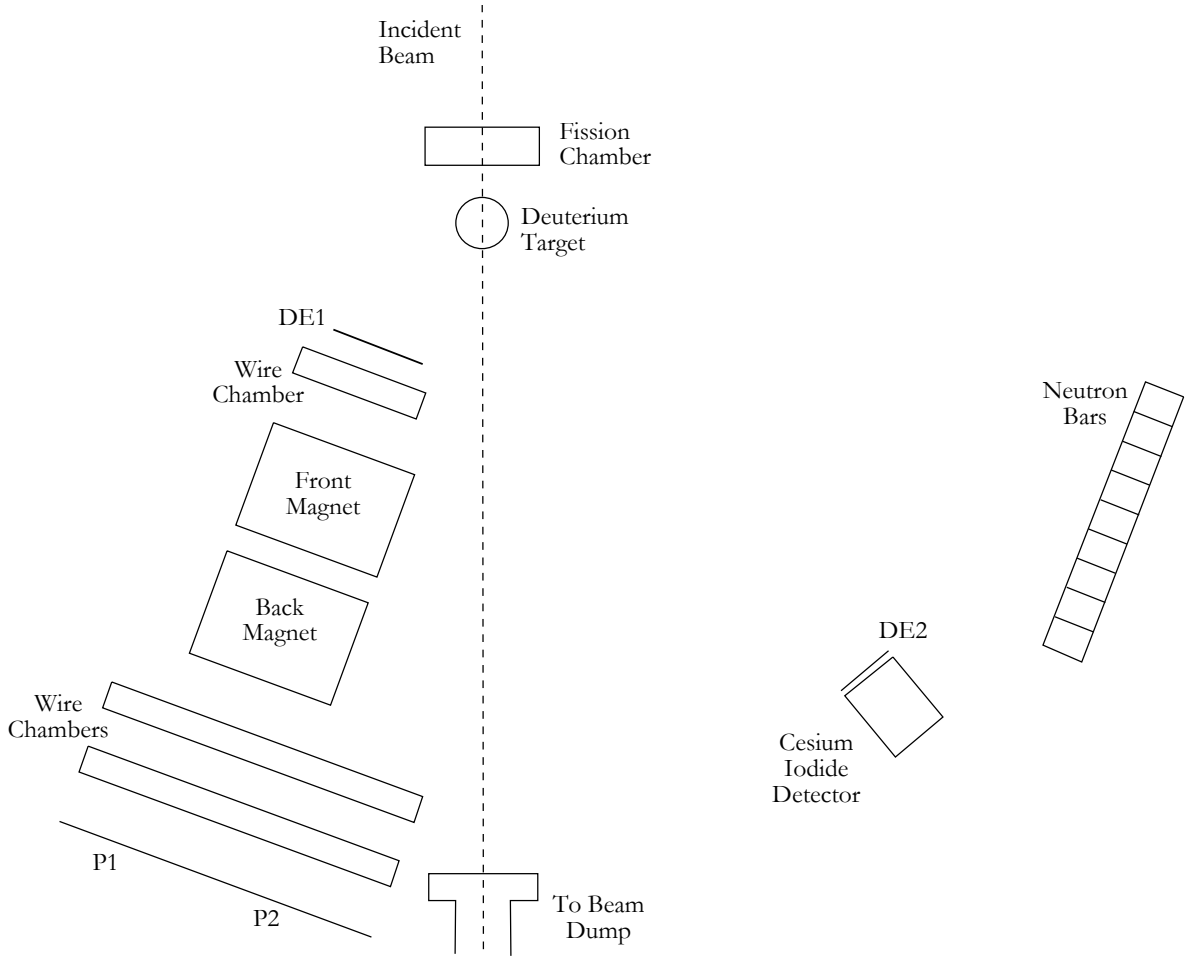

Figure 1.2 Schematic of experimental setup. Not to scale. Protons were detected to the right of the beam line and neutrons were detected in the neutron array located to the left of the beam line. The elastic monitor, consisting of a ΔE scintillator and Cesium Iodide detector, was located at about 40° to beam left.

where dA is an area element of the detector and r is the distance from the target to the area element. For a detector covering a full sphere, the solid angle is 4π.

The cross section $\sigma(\theta)$ can be found from Eq. (1.2):

$$\sigma(\theta) = \frac{1}{N_{inc}N_t}\frac{dN_d}{d\Omega}. \tag{1.3}$$

In the $n-d$ breakup experiment, both the neutron and the proton were detected in coincidence at different angles by detectors with different solid angles, so a doubly differential cross section may

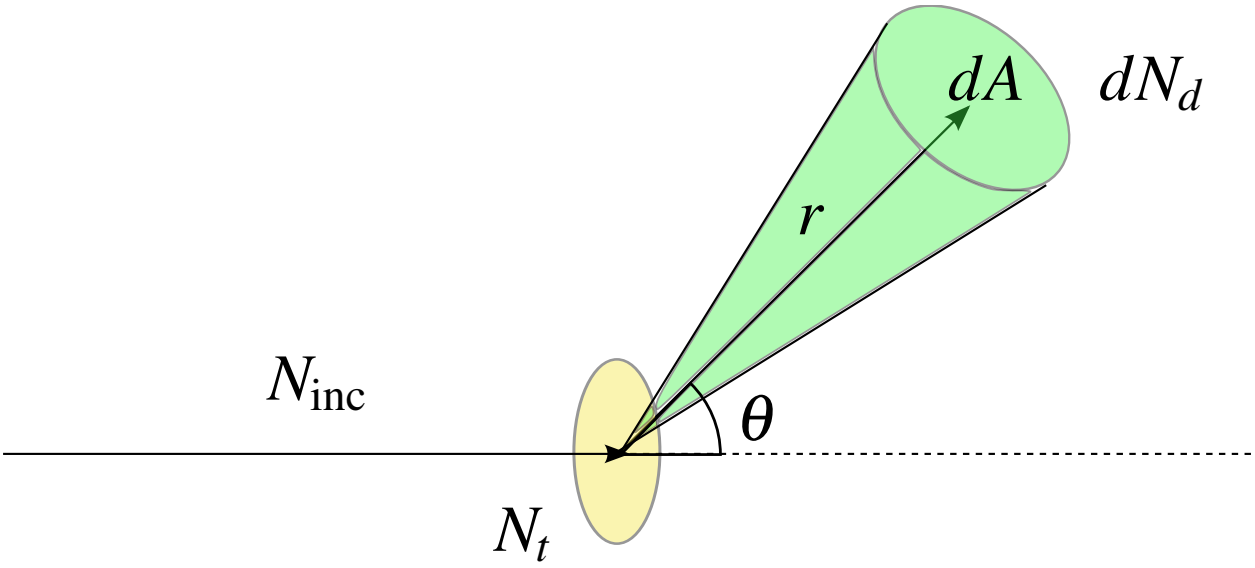

Figure 1.3 The incident particles coming from the left scatter from the target located at the center into the detector located in the upper right corner. The number of detected particles (dN_d) is proportional to the incident flux (N_{inc}), the number of scattering centers in the target (N_t), and the solid angle $d\Omega = dA/r^2$.

be used:

$$\sigma(\theta_n, \theta_p) = \frac{1}{N_{inc} N_t} \frac{d^2 N_d}{d\Omega_n d\Omega_p}, \tag{1.4}$$

where θ_n and θ_p are the scattering angles for the neutrons and protons respectively. The cross section may further depend on the incident energy of the neutrons and the energies of the deflected protons and neutrons, giving a 5-fold differential cross section. The experiment was designed to measure each of these parameters.

1.3 History and Motivation

The $d(n,np)n$ experiment sought to explore possible three-nucleon contributions to the strong force using neutron-deuteron scattering. The strong force, one of the four fundamental forces of the universe, is responsible for holding nuclei together. The strong force is typically though to act between two nucleons, and has been described by two nucleon force (2NF) models such as the Bonn [1] or Nijm I, II, or Nijm 93 potentials [2]. In a system of three nucleons, the 2NF models

would predict the interactions between the nucleons in terms of pairwise interactions as seen in Figure 1.4. However, these models (with the exception of the Bonn potential) failed to accurately predict the binding energy of triton, which it underestimated by 10% [3]. These 2NF models also underpredicted the experimental binding energies for ^{3}H, ^{4}He, and higher mass nuclei up to A=8 [4]. Three nucleon force (3NF) models which include potentials such as Urbana IX [5] or Tucson-Melbourne [6] include an additional interaction between three nucleons, as well as including the 2NF effects (see Figure 1.5).

The ideal system to test these models would be a three body system like a neutron and deuteron. A three body system is the smallest system in which 3NF effects might appear. The neutron-deuteron system is preferable because it does not include Coulomb effects inherent in the proton-deuteron system, which have greatest effect at lower energies and forward scattering angles. Other possible indirect tests of the models would include the binding of three nucleon isotopes like ^{3}H and ^{3}He.

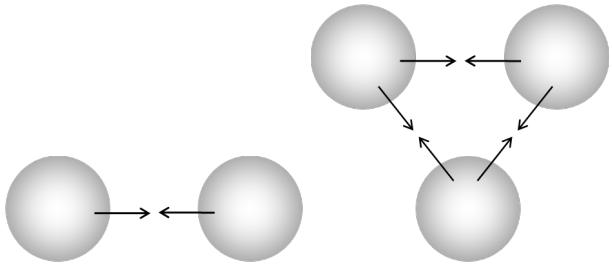

Figure 1.4 A cartoon of a two body interaction. On the left is a pictorial representation of a two body force. On the right is a system of three particles, where pairs of nucleons interact.

One possible method for testing 3NF models is neutron-deuteron elastic scattering. This can be seen in 1.6, which shows the 3NF predictions of Witala et. al. [10] as compared to measured $p-d$ scattering cross sections at incident energy of 200 MeV. Not only did the datasets disagree with one another, the data included Coulomb effects inherent in a system with a deuteron and proton. This was the motivation for the first scattering experiment to test 3NF models at the Los Alamos National Laboratory by our group in 2002 to measure the $d(n,nd)$ cross section. This cross section

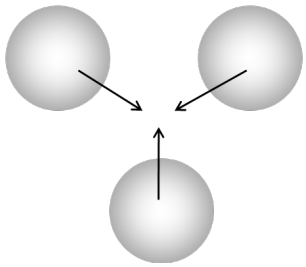

Figure 1.5 A cartoon of a three body interaction. The force is an interaction of three nucleons and may be present in addition to the pairwise interactions of Fig. 1.4.

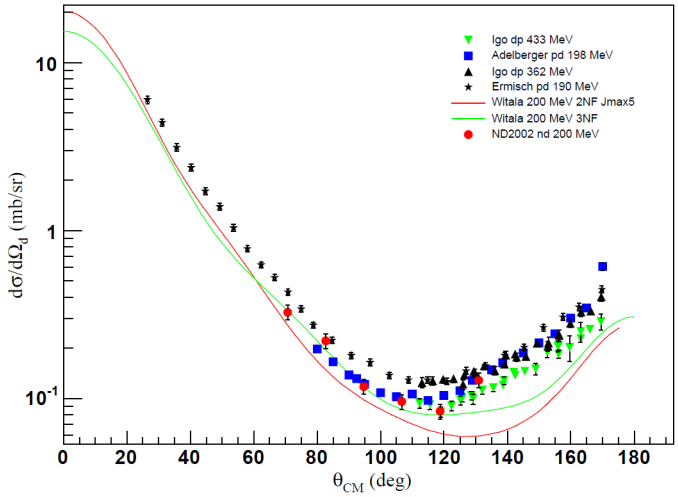

Figure 1.6 The neutron-deuteron elastic scattering cross section for incident neutron energy of 200 MeV as a function of θ_{CM}. The 2002 data (red circles) can be compared to other experimental measurements [7–9] and theoretical predictions (the green and red lines) [10]. The previous measurements did not agree with one another. Neither the 2NF model, nor the model including 3NF effects, accurately predicted the cross sections, based on these previous measurements. Therefore, the 2002 data was taken to improve previous measurements and test the theoretical models. The 3NF predictions agree more closely with the 2002 measurements than the 2NF predictions. Taken from Ref. [11]

was measured at incident neutron energies ranging from 140 to 240 MeV in 20 MeV increments and scattering angles in the center of mass frame from 24° to 54° in 6-degree increments [11]. The experimental setup can be seen in Figure 1.7. These measurements can be seen in as the red circles in Figure 1.6. The result of this experiment seemed to validate the 3NF models.

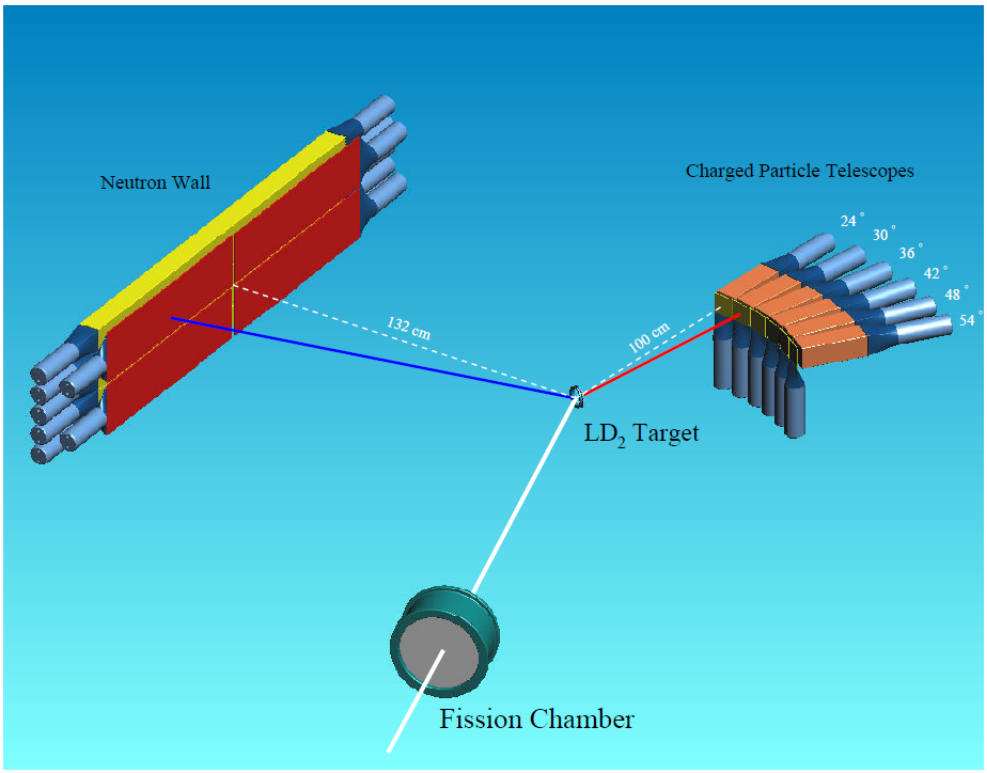

Figure 1.7 A schematic of the experimental setup for 2002 elastic scattering. The incident neutron beam hit the liquid deuterium target, after passing through a fission chamber used to normalize incident neutron flux. Elastically scattered deuterons were detected in charged particle telescopes on beam right and neutrons were detected on beam left. The ΔE detectors in the charged particle telescopes were used for particle identification and the detector paddles in front of the neutron wall were used as veto detectors, to throw out events where particles other than neutrons were detected by the neutron wall. Taken from Ref. [11]

The experiment was then extended to look at the breakup reaction $d(n,np)n$. Joanna Kuroś-Żołnierczuk's study [4,12] of the three nucleon force in 2002 had insufficient data on $N-d$ breakup

reactions to which she could compare her theoretical predictions. She compared three theoretical models—a 2NF model and two models which also included 3NF effects—to experimental data. Although her calculations are primarily in the non-quasielastic region, she did look at quasielastic regions as well.

Results from her analysis, seen in Figure 1.8, show that the greatest difference between the 2NF and 3NF predictions for cross sections occurs at far forward angles or the case where one particle is detected at a far forward angle and the second is detected at a backward angle. The largest difference between the two models comes when both particles are detected on the same side of the beam. Finally, higher outgoing energies show a larger difference between the two models. Experimental studies seeking results to distinguish which model is correct should be done with these kinematics.

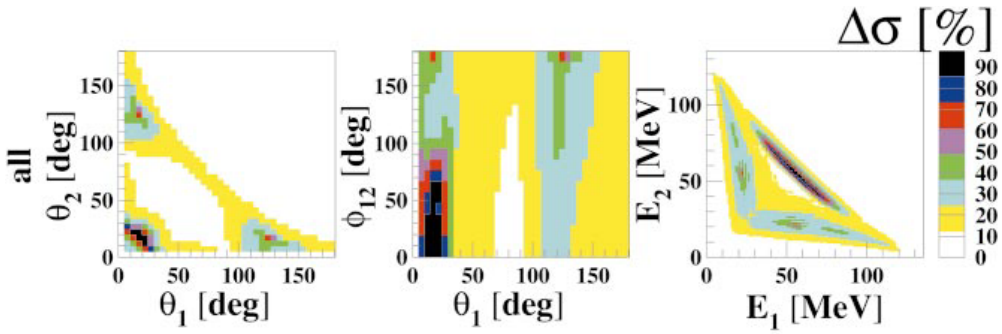

Figure 1.8 Histograms of the best kinematics for testing 2NF and 3NF models. In these plots, θ_1 and θ_2 are the scattering angles of the neutron and proton from neutron-induced deuteron breakup, ϕ_{12} is the azimuthal angle, and E_1 and E_2 are the scattering energies of the neutron and proton. In the first histogram, it can be seen that the difference between the 2NF and 3NF cross section predictions ($\Delta\sigma$) is higher at far forward angles (both θ_1 and θ_2 are low) or when one of the particles is detected at a more backward angle. The second histogram shows that detecting both particles on the same side of the beam (the azimuthal angle Φ_{12} is low) also yields a higher difference between 2NF and 3NF predictions. The third histogram shows that higher energies show an increased difference in 2NF and 3NF models. Taken from Ref. [4].

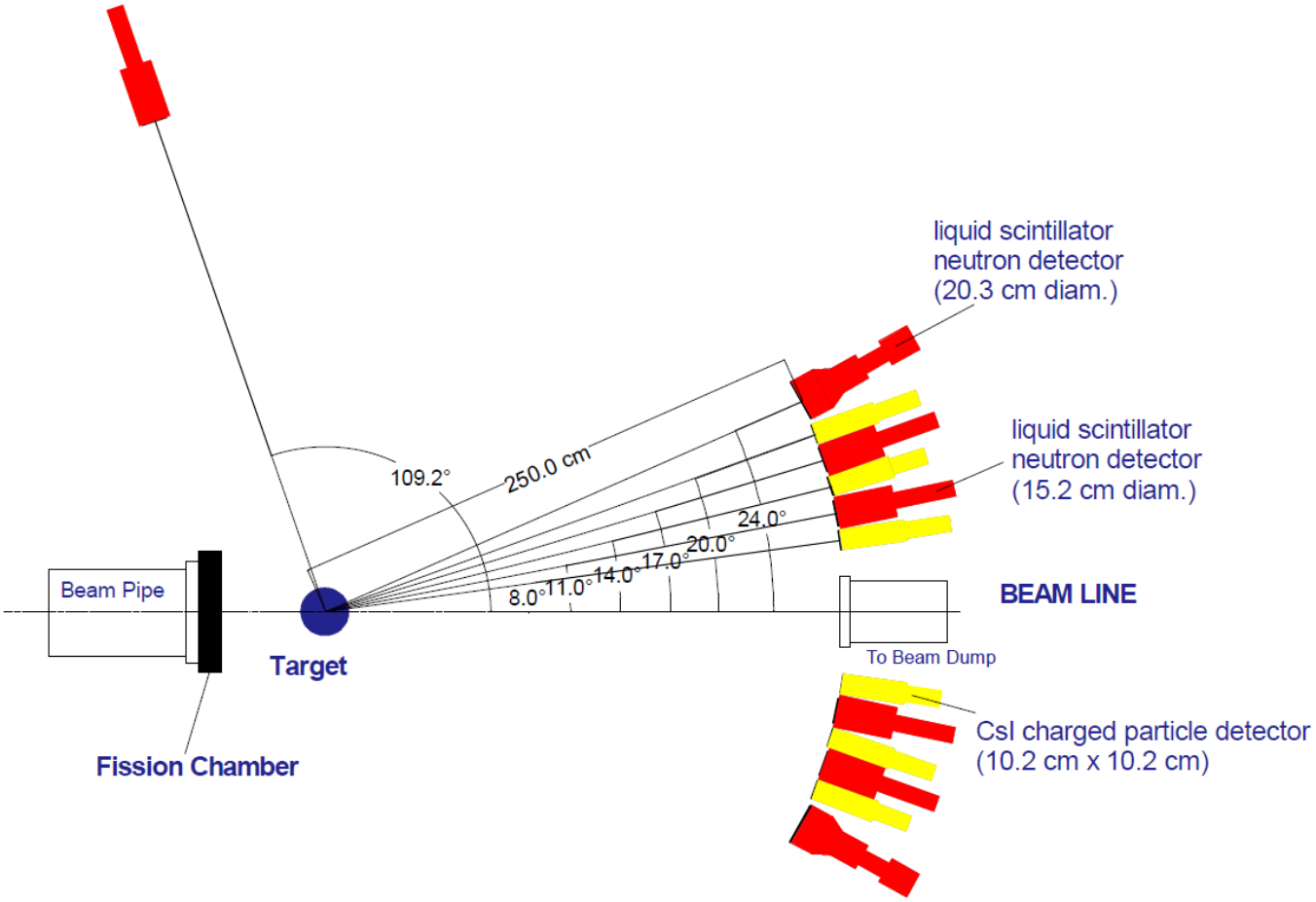

Figure 1.9 A schematic of the experimental setup used in 2003. The experiment was designed to detect scattered protons and neutrons at various angles, including on the same side of the beam, since these kinematics have the greatest discrepancies between predictions with and without 3NF effects. The experiment encountered the problem of particles scattering from detectors into other detectors, making the setup unusable for cross section measurements. Taken from Ref. [13].

The quasielastic region was found to have little 3NF sensitivity [4], so other kinematics were from 2003 to 2005, as seen in Figure 1.9. This experiment required a 100 Hz beam to get the necessary statistics, but only a 40 Hz beam was available, so in 2007 the group gave up the idea of

looking for 3NF effects and turned to look at quasielastic deuteron breakup since the cross section for the quasielastic region is much higher [14].

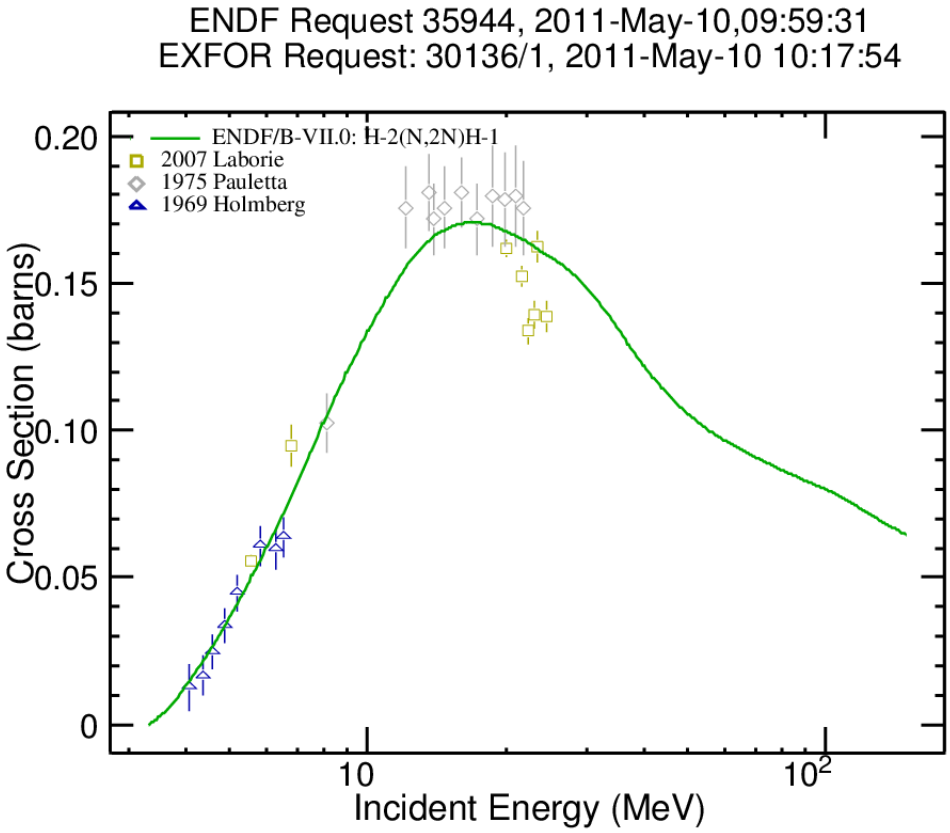

Figure 1.10 Total $n-d$ breakup cross section as a function of incident neutron energy. All previous measurements [15–17] for incident neutron energy less than 40 MeV. At the LANSCE facility, the neutron energy spectrum goes up to 800 MeV, which allowed cross sections to be measured for a range of incident neutron energies. Plot made using ENDF/B-VII.0 [18].

In 2007, a feasibility study for a measurement of the quasielastic $d(n,np)n$ reaction was performed. As of 2007, there were no previous measurements of the $d(n,np)n$ reaction at intermediate energies, as can be seen in Figure 1.10. There was one measurement performed at the Indiana University Cyclotron Facility (IUCF) [19] of the $d(p,pn)p$ cross section at 200 MeV, which in-

cluded quasielastic kinematics. The theoretical calculations by Kuroś-Żołnierczuk et. al. of two 2NF+3NF models did not agree with the results of this experiment as seen in Figure 1.11, although the discrepancies may be due to relativistic effects, which were ignored [12].

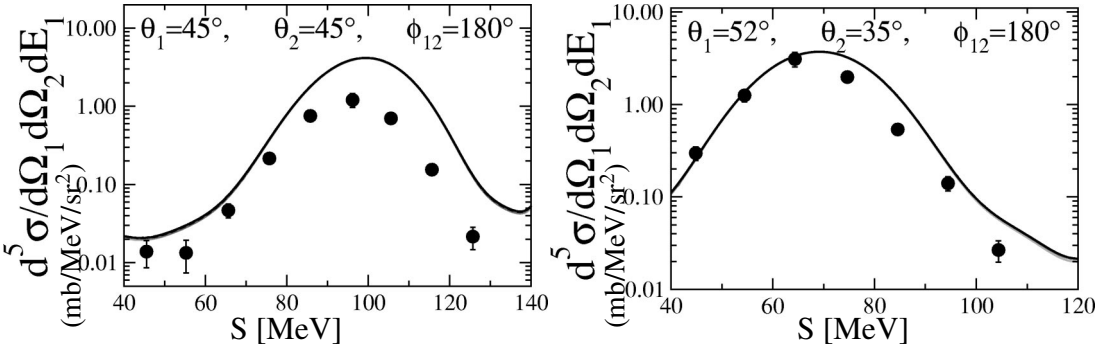

Figure 1.11 $n-d$ breakup cross sections at $E_n = 200$ MeV compared to 2NF predictions (light grey) and 3NF predictions (dark grey). The two theoretical calculations match so closely for these kinematics, they cannot be distinguished. θ_1 and θ_2 are the scattering angles of the incident and scattered proton and Φ_{12} is the azimuthal angle between the scattered nucleons. The x-axis represents points along the S-curve (in MeV), which is the kinematically allowed correlation between the scattered energies of the two nucleons [20]. The experimental cross sections are from Pairsuwan, et al [19]. While the general shapes of the cross section theory curves match the experimental data, the magnitudes do not. Taken from Ref. [12]

The 2NF and 2NF+3NF models were also compared to $p-d$ breakup cross sections at lower energies, since other $n-d$ measurements were only available at very low incident energies (10-15 MeV) [3, 21–23]. Of these experiments, only that done by Howell et. al. [22] specifically looked for quasielastic breakup. There were a few pd breakup measurements [24–27] at the higher energy of 65 MeV, all of which were conducted at quasielastic kinematics except one [24]. As can be seen in Figure 1.12 and Figure 1.13, theoretical predictions by Kuroś-Żołnierczuk et. al. were consistently too large for $p-d$ breakup with incident energies of 13 MeV and 65 MeV, although arguably Coulomb force effects were responsible for much of the discrepancy [12].

Other experiments looking at $p-d$ breakup at 130 MeV [30, 31] were conducted in non-

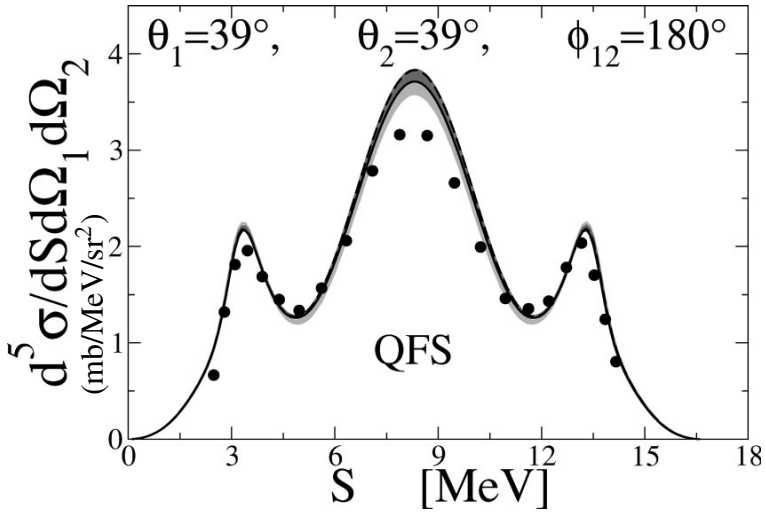

Figure 1.12 $p-d$ breakup cross sections at an incident proton energy of 13 MeV compared to 2NF predictions (light grey) and 3NF predictions (dark grey). See Fig. 1.11 for a descriptions of axes. In this plot, the theoretical maxima over-predicts experimental data [28], possibly due to Coulomb force corrections [12]. Taken from Ref. [4].

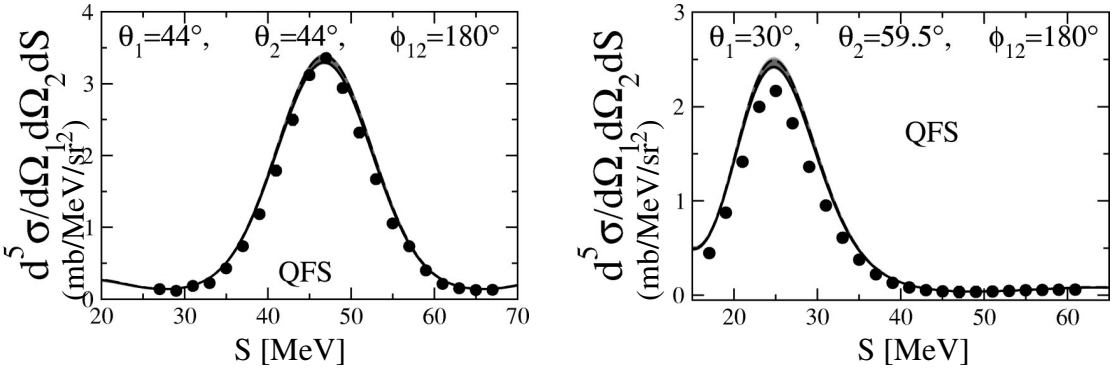

Figure 1.13 $p-d$ breakup cross sections at $E_p = 65$ MeV compared to 2NF predictions (light grey) and 3NF predictions (dark grey). See Fig. 1.11 for a descriptions of axes. While the general shapes of the cross section theory curves match the experimental data [29], the magnitudes do not. Taken from Ref. [12].

quasielastic regions to compare 3NF models and 2NF models. Both of these concluded the 3NF models increased the cross section predictions, which aligned them more closely with experimental

results.

Upon analysis of the quasielastic breakup data collected in 2007, there were too few events for the desired 5% accuracy, since one of the proton detectors was not working properly and there was insufficient beam time. The resulting preliminary cross sections can be seen in Figure 1.14. This analysis did not include detector efficiency analysis nor deadtime corrections and the scattering centers was estimated using stoichiometry rather than normalization to $n-p$ scattering data [32].

The experimental setup used for the 2007 experiment was used again in 2009 to look at quasielastic scattering in the neutron-deuterium experiment to increase the statistical precision of the measurements. This experiment corrected some of the problems encountered in the previous experiments.

Changes made to the experiment for 2009 increased usable data. In 2007, the data collected from one of the rear proton detectors (P2) were unusable because the detector was not working correctly. Further, a second wire chamber was added between the permanent magnets and the rear proton detectors to improve the accuracy of the proton path and thereby eliminate some of the uncertainty in the proton's momentum. Two horizontal scintillators were moved in front of the neutron bars to aid in neutron bar height calibration.

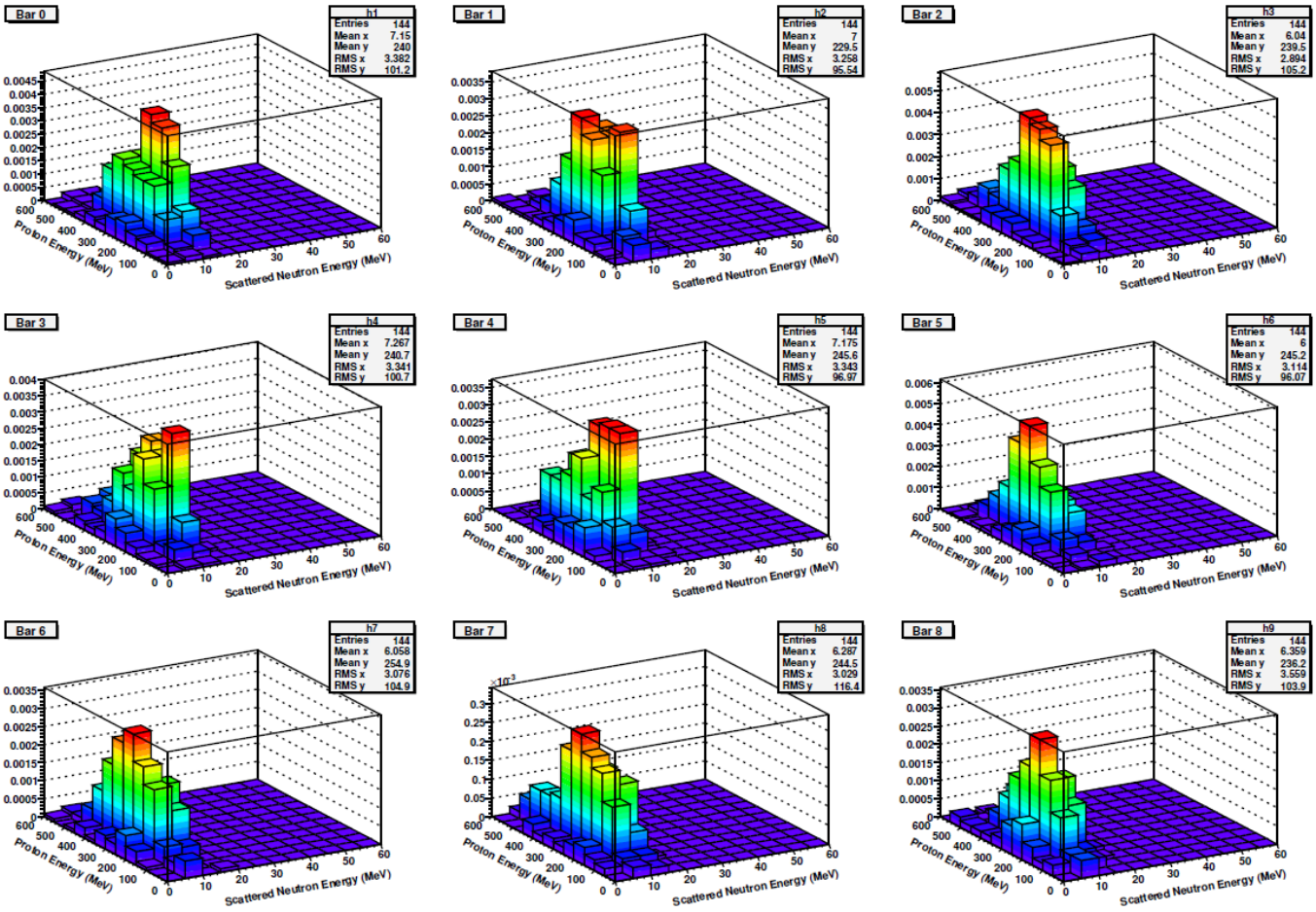

Figure 1.14 Preliminary differential $d(n,np)n$ cross section, $\frac{d^4\sigma}{dE_p dE_n d\Omega_p d\Omega_n}$ in mb/sr^2/MeV^2 for 300 MeV incident neutron energy, from the 2007 feasibility study is shown with each plot an approximately 2° bin for outgoing neutron angle. Each "bar" corresponds to 2-m high, 10 cm cross section detector left of the beamline. This array of detectors subtended 21°, starting 55° off the beamline. The cross sections for each plot are further binned by scattering neutron and proton energies. Taken from Ref. [32].

Chapter 2

EXPERIMENTAL SETUP

2.1 Overview

The $d(n,np)n$ experiment used the high energy neutron beam delivered to the Weapons Neutron Research (WNR) facility at LANSCE. The experiment was set up to detect scattered neutrons and protons in coincidence from the neutron beam striking a liquid deuterium target. As seen in Figure 1.2, the scattered protons were detected in a magnetic proton spectrometer to the right of the beam line. A "wall" of plastic scintillators for neutron detection was located on the opposite side of the beam line at the conjugate angle for quasielastic scattering to the proton detectors. The intention was to use the magnetic spectrometer to measure the energy of the scattered proton, from which the time of the scattering event could be calculated. Using time of flight, the energies of the incident and scattered neutrons could be determined, allowing the differential cross section with respect to energy to be calculated.

2.2 Neutron Beam

The pulsed incident neutron beam was produced using the 800 MeV, 860 nA pulsed proton beam from the Clinton P. Anderson linear accelerator (linac). The protons strike a tungsten spallation target, producing neutron beams for various experimental areas [33, 34].

2.2.1 Linear Accelerator

The linac at LANSCE can accelerate positive and negative hydrogen ions up to 800 MeV. Two 750 keV Cockcroft-Walton ion generators strip electrons off hydrogen atoms to make H^+ and add electrons to other hydrogen molecules to make H^-. The 750 keV energy hydrogen ions are injected into the second stage of the accelerator, the Alvarez Drift Tube Linac [34], in alternating bunches of H^+ and H^- ions, where the 201.25 MHz drift tube alternates polarity to accelerate the ions up to 100 MeV, as can be seen in Figure 2.2. The ions accelerate in the space between the drift tubes and the tubes increase in length, so the ions spend the same amount of time in each tube, allowing the polarity to be switched at a regular rate.

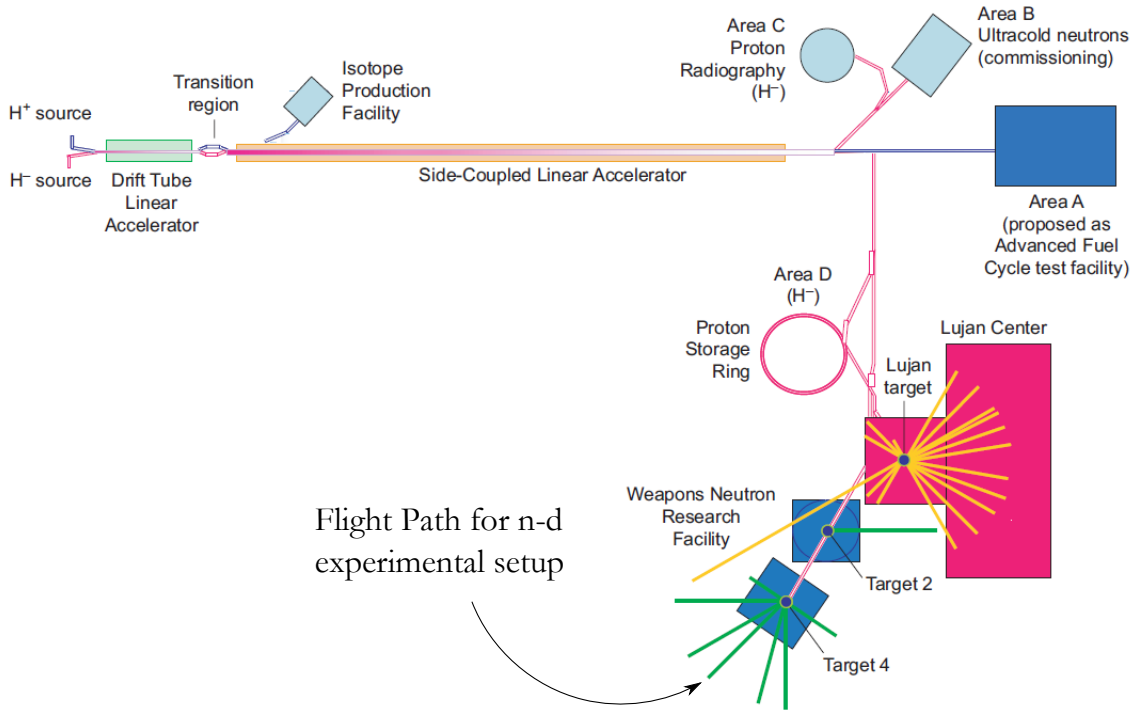

Figure 2.1 Schematic of the accelerator at LANSCE. Not to scale. Hydrogen ions from the H^+ and H^- ion sources are injected into the drift tube linac, where they are accelerated up to 100 MeV. Then, they go through the side-coupled linear accelerator, where they are further accelerated up to 800 MeV. They can then be diverted into the Proton Radiography area, Ultra-Cold Neutron area, or toward the Lujan Center and the Weapons Neutron Research Facility. The red lines are the paths of the negative hydrogen ions and the blue lines are the paths of the positive hydrogen ions. The $n-d$ experiment was located 15° to the right of the beamline, as labeled in the figure. Taken from Ref. [35].

The drift tubes accelerate the hydrogen ions up to about 100 MeV, after which they are either used at the Isotope Production Facility or go on to the 800-m long side-coupled linear accelerator, which works similarly to the drift tubes but with 800 MHz rf. The side-coupled linear accelerator further accelerates the hydrogen ions up to 800 MeV [34]. These ions may be used in a few different facilities including the Proton Radiography area and the Ultra-Cold Neutron area, as

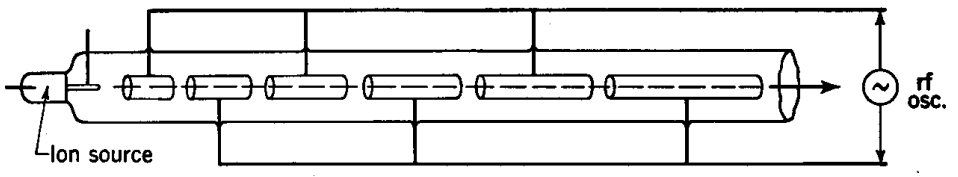

Figure 2.2 Schematic of a typical drift tube linac. Alternating polarity on the drift tubes cause the ions to accelerate. Figure from Ref. [36].

shown in Figure 2.1. The negative ions used for the production of the neutron beam make a ninety-degree turn beneath a road, where they can be used at the Lujan Center, where a moderator is used to produce slow neutrons, or at the WNR facility, where the $n-d$ experiment was located.

2.2.2 Neutron Beam Production

Positive hydrogen ions strike a water-cooled 3 cm diameter tungsten spallation target [37], called Target 4, as indicated in Figure 2.4. This cylindrical target is 7.5 cm long and is suspended in a vacuum chamber. An average of 860 nA of current was incident on the tungsten target. The result of the pulsed proton beam (see Figure 2.3) is neutron pulses at 40 Hz. Each of these macropulses contains 200 ps micropulses separated by 1.8 μs or 3.6 μs [1] [38].

The resulting neutrons are collimated in a 108-in long iron collimator [11]. The beam is shuttered with depleted uranium and iron sleeves that fit into the collimator and were used to reduce the beam size to a 1.5 in diameter. See Ref. [37] for more specifics on neutron beam production.

The resulting neutrons are not monoenergetic, ranging from below a few MeV up to approximately 800 MeV. The neutron energies could be determined using TOF, since the beam was pulsed. Knowing when the proton bunch hit the spallation target (the 0.2 ns duration of the proton pulse was sufficiently short enough for the energy resolution required), the arrival time of the neutrons at the target, and the flight distance allowed for TOF calculations. The spallation target provides

[1] During the deuterium target runs in August, the pulse spacing changed for about a week from 1.8 μs to 3.6 μs spacing.

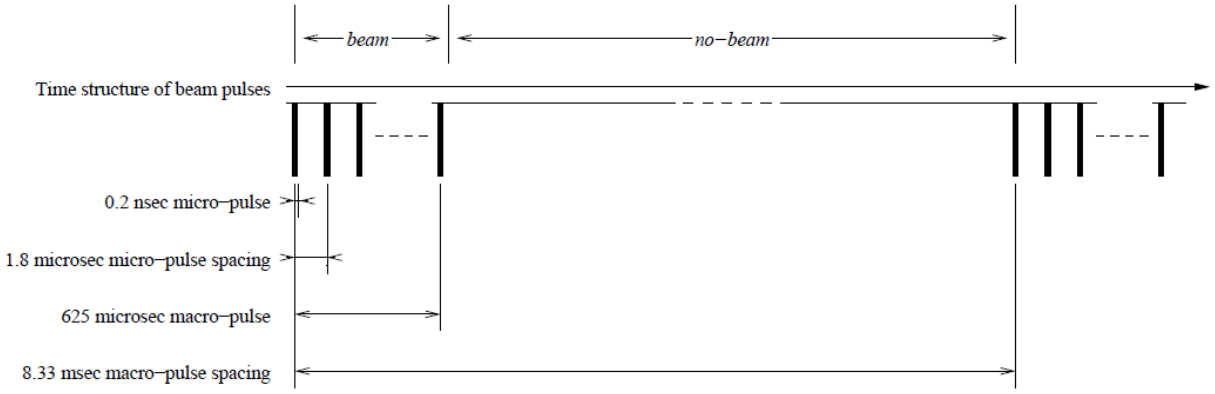

Figure 2.3 The time structure of the pulsed beam. The short pulse width and 1.8 μs spacing between pulses allows precise time of flight measurements without micropulse overlap. Figure from Ref. [11].

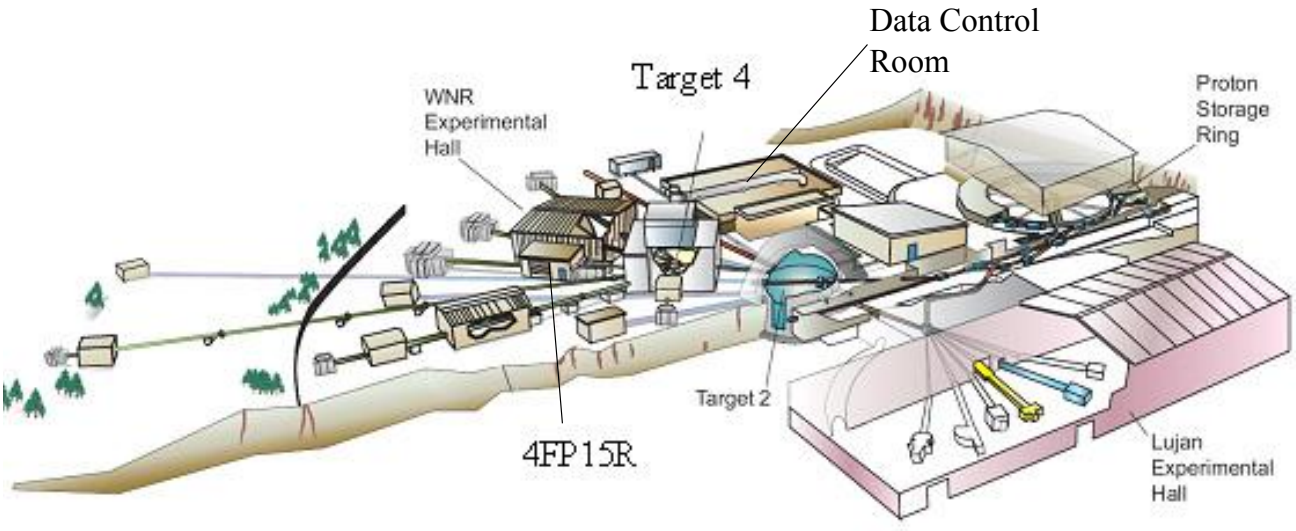

Figure 2.4 The WNR layout. The WNR Facility houses two spallation targets Target 2 and Target 4, upon which the proton beam supplied by LANSCE may be incident. The proton beam enters at right and the experimental area for this experiment was 4FP15R. Figure from Ref. [35].

neutron beams for several experimental areas including 4FP15R, where this experiment took place, 15° to the right of the proton beam line and 16.93 m downstream of Target 4.

To determine the size, position, and intensity of the beam spot, several beam profiles were measured using FUJI storage-phosphor image plates. The plates store neutron intensity information upon being bombarded by incident neutrons. The nuclear-chemical reactions are reversible under light exposure, so a scan with a laser beam reverses the process, emitting photons which are captured by a photo-detector. This process happens in a digitizer-drum, which yields a beam profile image.

These images were taken in two places–one right after the collimator before the fission chamber and one downstream of the deuterium target by about 130 cm. The plates used to capture the beam profile for this experiment were exposed for approximately 35 minutes.

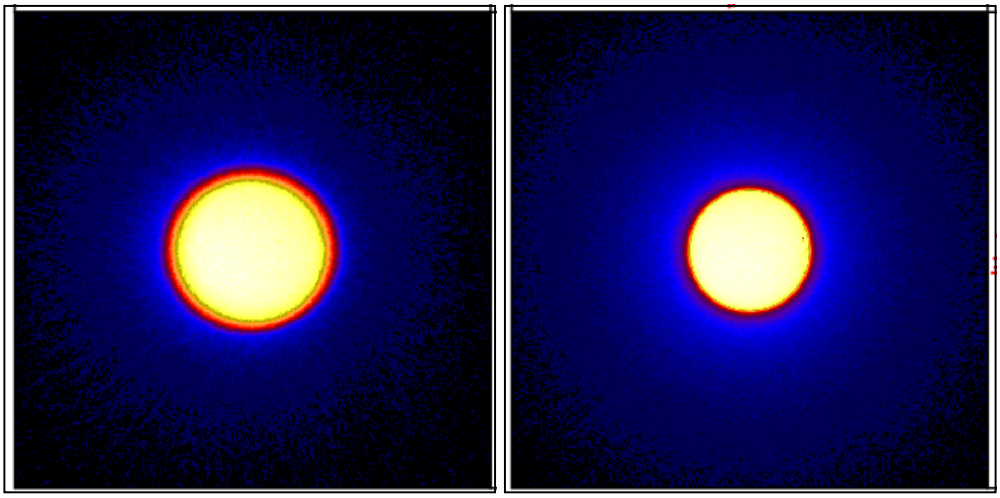

Figure 2.5 Beam profile from image plates. The left picture is of the beam spot right before the fission chamber and the right is downstream from the deuterium target by about 130 cm. These were used to determine the absolute position of the beam as well as the intensity of the beam profile. The dark blue shows lower intensity, whereas the white-yellow colour shows higher intensity. There is no absolute scale, however, so only relative intensity can be discerned.

2.3 Fission Chamber

To normalize the data collected in the experiment, the incident neutron flux was measured using a fission chamber. The incoming neutrons caused the ^{238}U contained in the enclosed cylindrical fission chamber to fission, releasing fission fragments, which ionized the gas in the chamber. The number of electrons from the ionized gas were proportional to the energy of the ionizing particles, allowing the fission events to be selected from the background of alpha particles. Since the fission cross section of ^{238}U is known, the neutron flux could be measured.

The fission chamber used in the $n-d$ experiment was a horizontal cylinder (29.2 cm in diameter) with one of the eight steel foils lined with ^{238}U. The uranium deposit was electroplated by Isotope Products Laboratories to the back of a 0.013 mm-thick aluminum-coated steel foil [33] with an areal density of 0.908×10^{-6} atoms/barn [11]. The area not exposed to the beam was masked, so alpha particles were not detected from the sample not in the beam path [33].

The fission fragments ionized the 90% argon-10% methane gas mixture contained in the chamber at 69 kPa, and the electrons were collected on foil 3 separated 0.51 cm from the uranium deposit as shown in Figure 2.6 [11]. A 290 V difference between the foils attracted the electrons. The foils across from the deposits collected the electrons [33], which were read into a time-to-digital converter (TDC) and analog-to-digital converter (ADC), so the TOF and pulse height respectively were recorded. As is evident from Figure 2.7, the pulse heights could be used to distinguish the ionization pulses from the alpha particles and the fission fragments. The TDC information was used to calculate the TOF of the incident neutron, so the incident neutron energies could be found.

The TOF information for the fission chamber was found using the T_0 pulse sent from Target 4, explained more fully in Section 2.8.3. The T_0 pulse was used as a start trigger and the timer was stopped when fission was detected. This was possible because the TDC could reset itself on the next start signal if it received no stop trigger. Since the T_0 pulse was used a start trigger, the spectrum was inverted as seen in Figure 2.8. Here, high TDC channels correspond to faster times, so the photons from the spallation target are faster and appear on the far right.

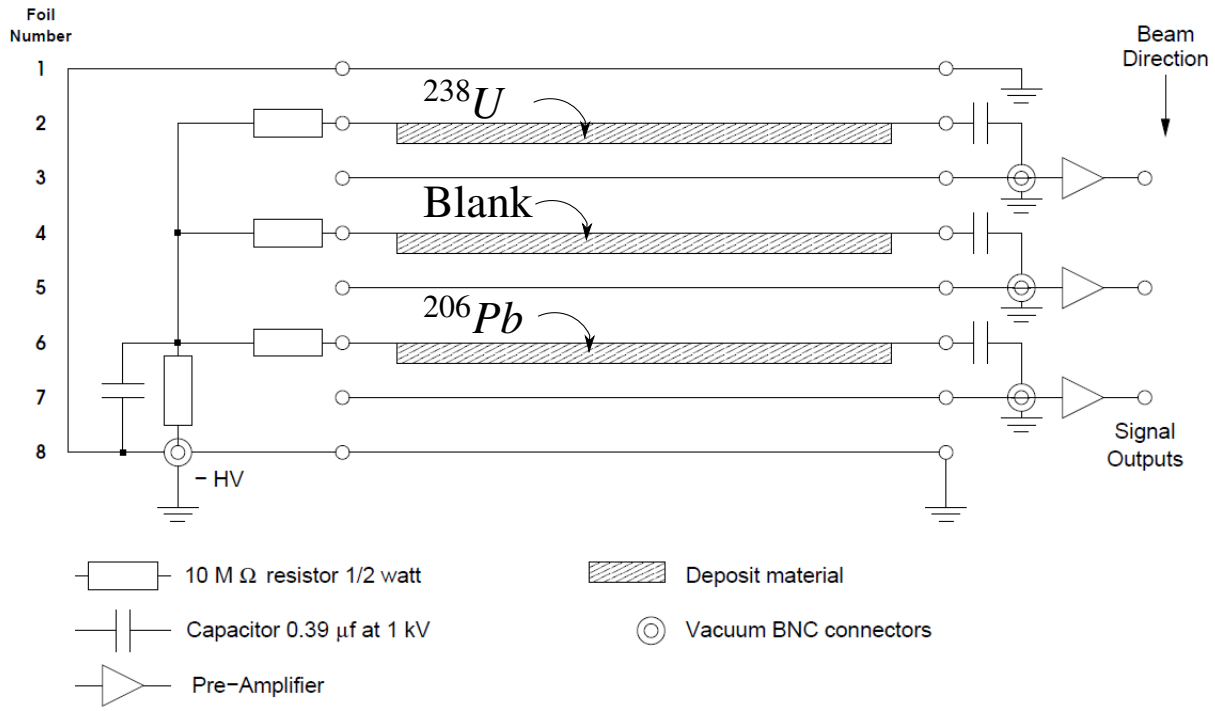

Figure 2.6 Electronic diagram of the fission chamber. The first foil had a deposit of ^{238}U, the second foil was left blank, and the third foil had a deposit of ^{206}Pb. Foils 1 and 8 were grounded and foils 3, 5, and 7 were used to collect electrons from the ionized gas. Figure from Ref. [33].

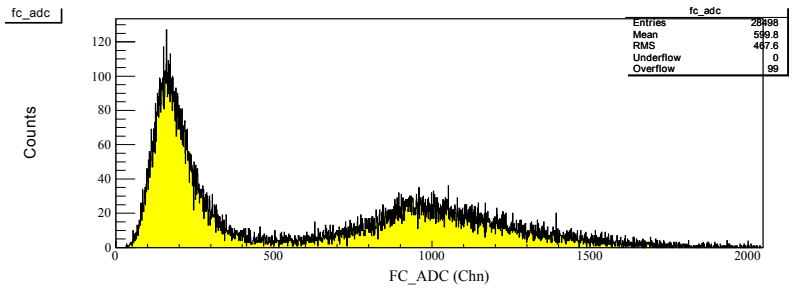

Figure 2.7 Fission chamber pulse heights. This spectrum of the raw ADC output in channels for the fission chamber shows two peaks. The first peak corresponds to alpha particles and the second peak corresponds to fission fragments.

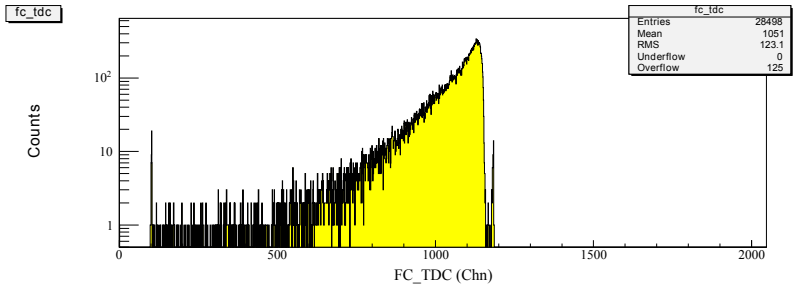

Figure 2.8 Fission chamber TDC spectrum. This spectrum of the raw TDC output in channels for the fission chamber. The peak on the far right corresponds to the gamma flash from Target 4.

2.4 Target

The liquid deuterium $\left({}^2\mathrm{H}\right)$ target was contained in a 1.27-cm long horizontally-oriented cylindrical flask with 50.8 μm thick mylar faces. The deuterium began in gaseous form, which was purified by a liquid nitrogen trap and oxygen filter after being cooled down with a CTI Model 1020 cooler. The deuterium was liquefied in a condensing chamber, where it collected in the 12.7-cm diameter deuterium flask located at the bottom of the system. The flask containing the liquid deuterium was thermally insulated within a vacuum chamber (See Figure 2.10). The 4.76-mm thick stainless steel cylindrical vacuum chamber with approximately 32-cm diameter had 127 μm thick kapton windows [11].

Before filling the target with ${}^2\mathrm{H}$, the target was filled with liquid hydrogen, which was used to normalize the deuterium data. Toward the end of the experiment, empty target data were collected, so background events from target windows could be subtracted.

2.5 Magnetic Spectrometer

To the right of the beamline, the magnetic spectrometer consisted of a series of detectors set up to measure the energy and scattering angle of the scattered protons. The positions and dimensions of the detectors can be found in Table 2.1 and Table 2.2. The protons were detected by scintillators located at the front (ΔE1) and rear (P1 and P2) of the spectrometer. The relationship between

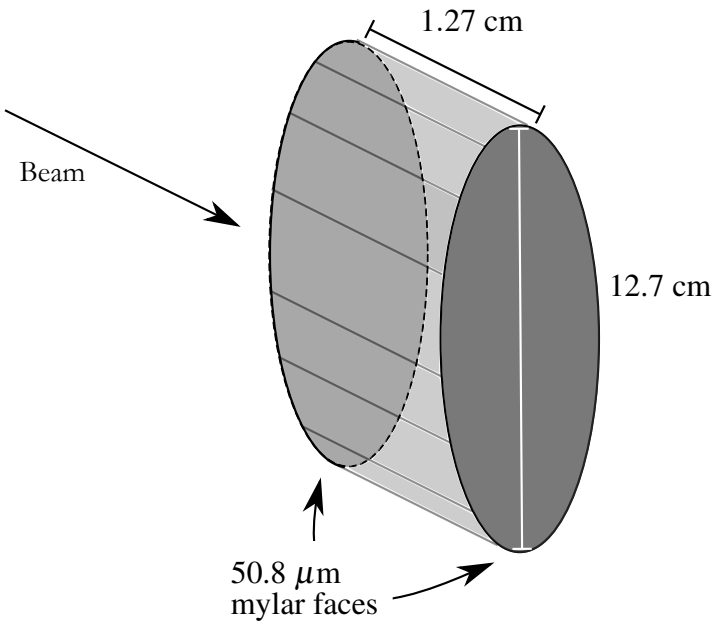

Figure 2.9 Schematic of deuterium target. The 12.7 cm diameter flask containing the deuterium had 50.8 μm thick mylar faces and total thickness of 1.27 cm thickness.

the energy lost in the initial and final scintillators could be used to separate proton events from those caused by elastically scattered deuterons or other particles. Magnets located at the center of the spectrometer deflected the proton's path, where the radius of deflection was determined by the proton's momentum. To find the curvature of the particle's path, wire chambers were used to determine the particle track before and after the magnets.

2.5.1 ΔE1 Scintillator

Protons coming from the neutron-deuteron reaction were first detected by a 2.5 mm-thick plastic ΔE scintillator with the inside edge located 14° to the right of the beam line. The detector was attached to a photomultiplier tube (PMT) via an acrylic light guide.

Scintillators work using luminiscence, i.e. when molecules in the scintillator interact with charged particles, they absorb some of the energy of the incident particle and re-emit that energy as light, which the photomultiplier tube can convert into electrical pulses as shown in Figure 2.11. The

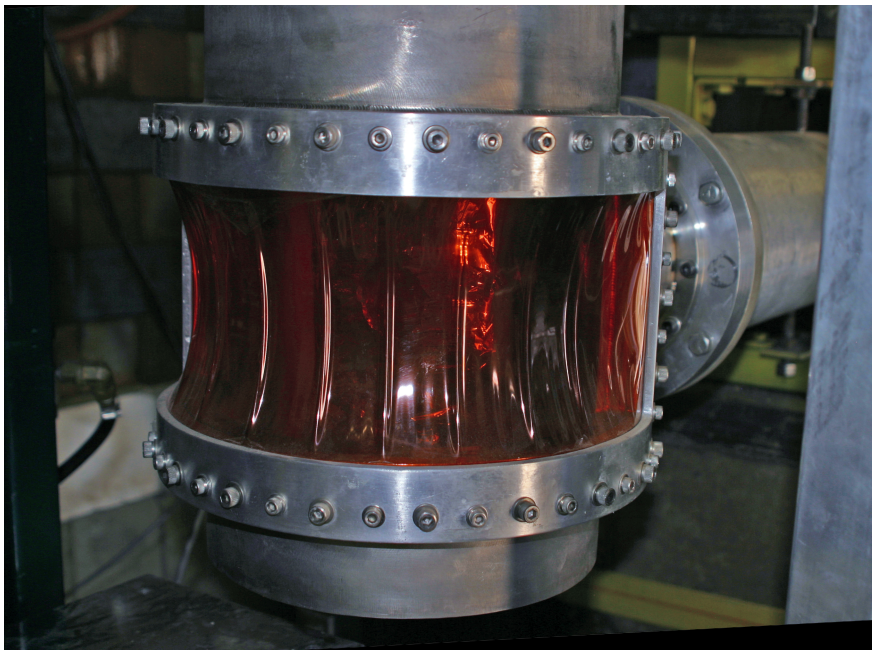

Figure 2.10 Photo of the deuterium target chamber. The deuterium target was contained in a vacuum chamber with orange kapton windows. The beam pipe is attached to the chamber at right in the photograph.

photon absorbed from the scintillator at the photocathode releases an electron via the photoelectric effect. This electron is accelerated toward the dynode, which is held at a high positive voltage. Because it is accelerated, it ejects more electrons which are in turn accelerated toward the next dynode. Each successive dynode is held at an increasingly positive voltage, which causes more and more electrons to be ejected creating an avalanche, so the pulse collected on the anode is amplified.

Because the ΔE detector was only 2.5 mm thick, neutrons were unlikely to interact with it because they are uncharged. Thus, particles detected in both the ΔE detector and the scintillators located at the rear (labeled P1 and P2 in Figure 1.2) were likely charged particles.

Table 2.1 Positions and Dimensions of the detectors and magnets in the magnetic spectrometer.

	Detector Width (cm)	Detector Height (cm)	Detector Thickness (cm)	Height from ground to top left front corner (cm)
ΔE1	15	32	0.25	149
WC1	33	48	15	164
PM1	48	21	30	NA
PM2	48	21	30	NA
WC2	79	43	7	150
WC4	79	43	7	150
P1	38	37	0.6	146
P2	38	37	0.6	146

Length measurements are ± 0.5 cm.

Angular measurements are $\pm 1^{\circ}$.

2.5.2 Wire Chambers

Behind the ΔE detector was a set of two drift chambers, which could be used to determine the flight path of the protons. Drift chambers contain planes of parallel wires oriented horizontally and vertically, which use ionization from charged particles passing through the gas in the chambers to reconstruct particle paths. The drift chambers had two sets of *x* and *y* planes, which collected the electrons when the 69% argon–31% isobutane gas mixture was ionized by a passing proton [32]. The drift chambers also contained isopropyl alcohol vapor, which was used to keep the wires clean.

Each pair of *x* and *y* planes allowed the coordinates of the proton to be pinpointed, so each wire chamber yielded two sets of *x*, *y*, and *z* coordinates, from which the straight-line trajectory of the proton could be found. The *z* coordinate came from the wire plane distance from the target. The wire chamber planes consisted of parallel anode wires held at around +2000 V. Centered between

Table 2.2 Geometry of the magnetic spectrometer.

	Distance to Target*		Angle between beam and inside edge of detector/magnet (°)	Angle subtended by by detector/magnet (°)
	Beam side (cm)	Outside (cm)		
ΔE	58	61	14	14
WC1	64	66	4	29
PM1	102	105	27	27
PM2	132	137	11	20
WC2	182	184	7	25
WC4	199	200	8	23
P1	220	219	8	10
P2	219	222	18	10

Length measurements are ± 0.5 cm.

Angular measurements are $\pm 1^{\circ}$.

*Distance from center of target to front face of detector/magnet.

the 8 mm-spaced anode wires were cathode wires held at ground, as shown in Figure 2.12 [39]. The wire chambers were sealed by a 6.3 μm thick mylar foil aluminized on both sides.

When the charged protons ionized the argon-isobutane gas mixture as they traveled through the wire chamber, the charge was collected on the anode wire closest to the track, and an induced pulse read on the nearest cathode wire. The anode wires were bussed together with a delay line and the pulse was recorded at each end of the plane, as shown in Figure 2.12. The time difference between when the signal reached each end of the delay line was used to determine which anode wire was closest to the event and the time sum was used to calculate the drift time. Using the cathode information, which allowed events to be categorized based on which side of the anode the particle passed, the position of the proton was expected to be accurately determined to within 100 μm.

Figure 2.13 shows a schematic diagram for a charged particle passing through a wire chamber

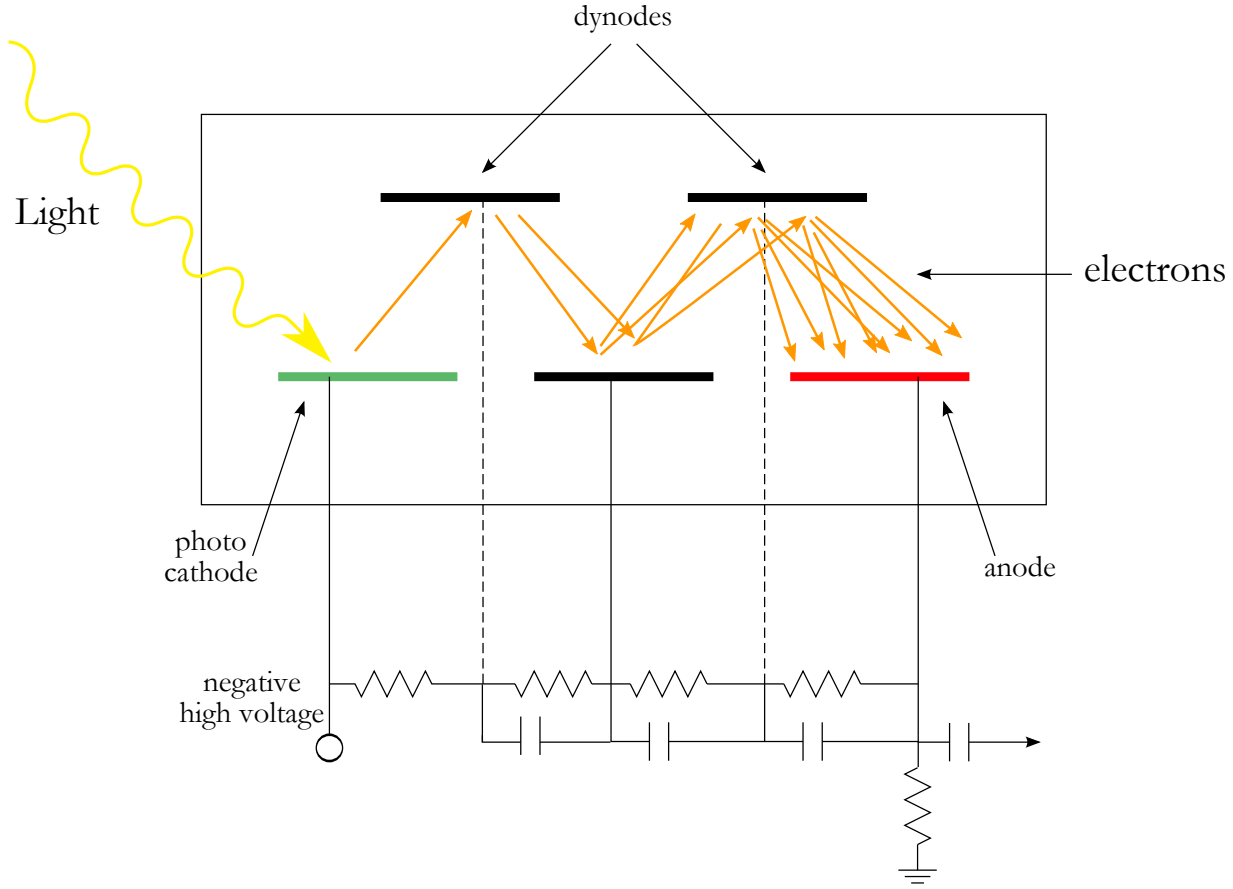

Figure 2.11 Schematic of a PMT. The photon striking the photocathode releases an electron. It is accelerated toward the dynode, due to a voltage difference, where it ejects more electrons. Due to the voltage differences across each dynode, the electrons avalanche and the amplified signal is collected on the anode.

plane. The times for the pulse to travel to the left (t_l) and right (t_r) end of the delay line is given by

$$t_l = \frac{d}{c'} + \frac{x}{c} \tag{2.1}$$

and

$$t_r = \frac{d}{c'} + \frac{D-x}{c}, \tag{2.2}$$

where D is the length of the delay line, x is the distance to the anode wire, d is the drift distance, c' is the drift speed of the electrons in the gas, and c is the speed of the pulse in the delay line. The

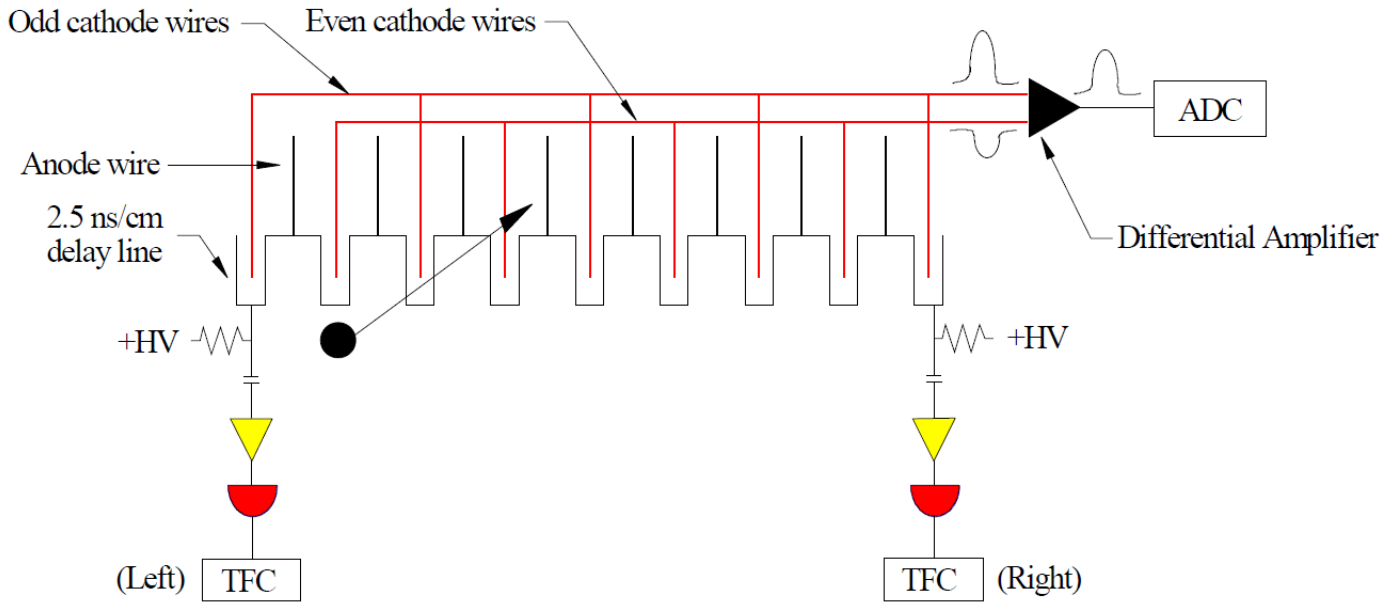

Figure 2.12 Schematic of a wire chamber plane. A charged particle passing through the plane ionized the gas, so it was possible to retrace its path based on which anode wire collected the ionization electrons. An induced pulse was also read from the cathode nearest the event, which could be used to determine whether the particle passed to the right or left of the anode. Figure from Ref. [39].

difference of these two times (t_d)

$$t_d = t_l - t_r = \frac{2x - D}{c}, \tag{2.3}$$

gives the position of the anode wire closest the event:

$$x = \frac{ct_d + D}{2}. \tag{2.4}$$

To convert these distances to absolute position in space, two small plastic scintillators were placed behind the magnetic spectrometer. The detector closest to beamline was 4 cm square with 0.5 cm thickness. The other detector was 7 cm tall, with 5 cm width and 0.3 cm thickness. Cutting the time difference spectra on the rear plastic fingers allowed wire position to be correlated to the absolute geometry of the experimental setup, as seen in Section 3.2.2.2.

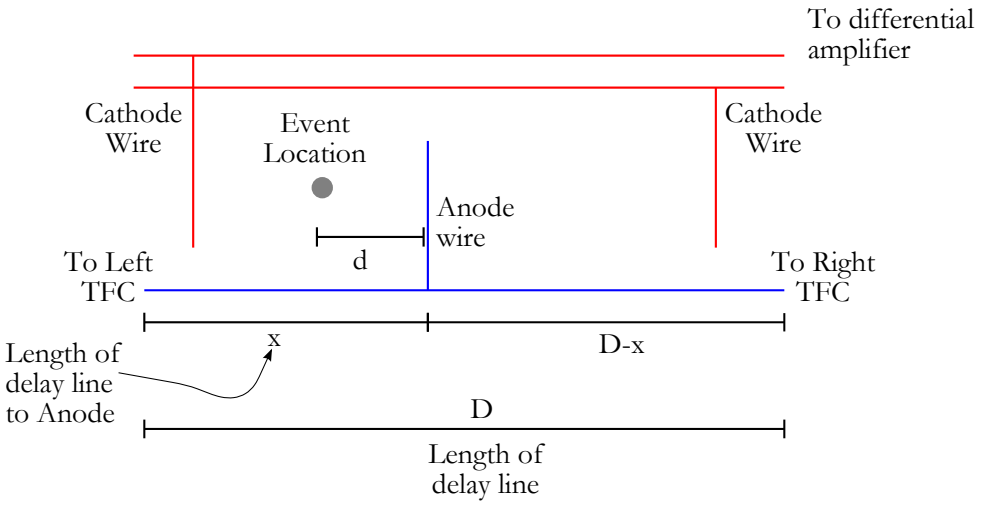

Figure 2.13 Schematic of a wire chamber event. The proton passed through the gas at a distance d from the anode wire, known as the drift distance, ionizing the gas. The electrons were collected on the nearest anode wire and the pulse traveled down to the delay line, where the signal split to the left and the right. Using the difference and sum of the times from each end of the delay line, the event position could be calculated.

The sum of these two times (Eqs. (2.5.2) and (2.5.2)) yields

$$t_l + t_r = \frac{2d}{c'} + \frac{D}{c}, \tag{2.5}$$

which gives the drift distance

$$d = \frac{c'(t_l + t_r - D/c)}{2} \tag{2.6}$$

so the time sum is linearly related to the drift distance or drift time $\left(t_d = \frac{d}{c'}\right)$.

It only remained to determine on which side of the wire the drift distance was. This was done using "odd-even" differential amplifiers. Depending on which cathode wire was closer to the event, the differential amplifier shown in Figure 2.12 output a positive or negative pulse. The raw ADC spectrum for an odd-even amplifier is shown in Figure 2.14. The two peaks correspond to events that occurred to the left and right of the anode wires. The exact position of an event could then be determined as the wire distance plus or minus the drift distance. To determine whether or not the drift distance needed to be added, the track distance for one plane was histogrammed against the

track distance for the plane immediately behind it. In this way, the smoothest distribution would be the correct combination of plus or minus. This method did not yield satisfactory results, likely due to the "odd-even" amplifiers not working. Rather than the 2-peak signature of a working "odd-even" amplifier seen in Fig. 2.14, the spectra of malfunctioning amplifiers had one peak, making it difficult to discern for which events the drift distance needed to be added or subtracted. As a result, about 20% were misidentified, so precise position tracking was not possible.

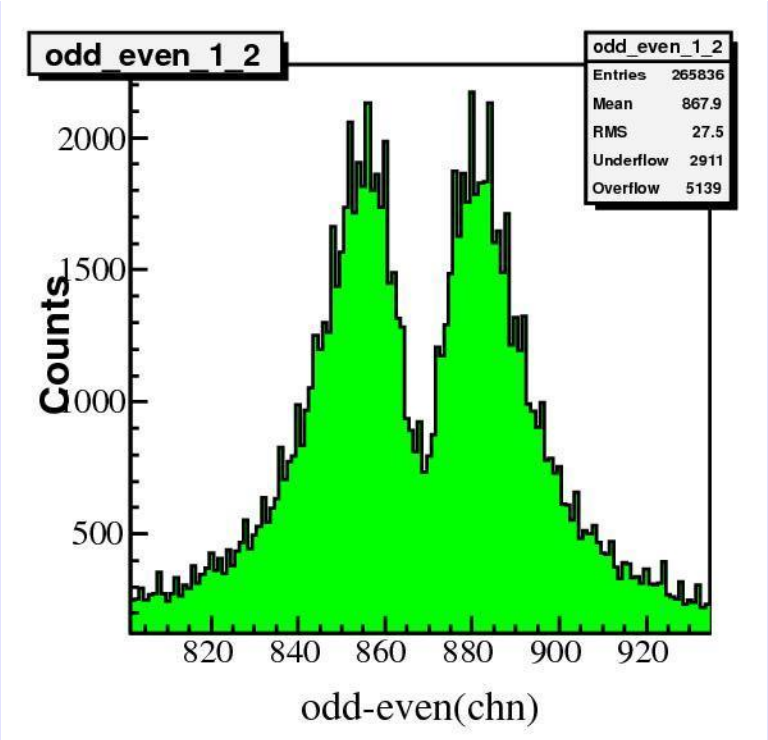

Figure 2.14 Histogram of the raw ADC output from odd-even amplifiers. The odd-even amplifiers output positive or negative pulses depending on whether the pulse came from an "even" or "odd" cathode. All the events on one side correlate to events which occurred to the right or left of the anode wire. This left-right ambiguity could be resolved by plotting the various combinations for two consecutive x or y-planes.

2.5.3 *Magnets*

Between the wires chambers, the proton beam was deflected by two 30 cm $\times$ 48 cm samarium-cobalt permanent magnets with a field strength of approximately 3000 G [40]. Using the Lorentz force, it is possible to find the proton's momentum in terms of known variables. A charged particle in the magnetic field experiences a force of

$$\vec{F} = q\vec{v} \times \vec{B}, \tag{2.7}$$

where q is the charge of a particle, $\vec{v}$ is its velocity, and $\vec{B}$ is the strength and direction of the magnetic field. This force causes the charged particle to travel in a helical path away from the beam line. Since the magnetic field of the permanent magnets pointed up, perpendicular to the proton's velocity, the proton experienced a centripetal acceleration. The force required to keep a particle traveling in a circle is

$$F = \frac{mv^2}{r}, \tag{2.8}$$

where r is the radius of the circle. Setting the centripetal force equal to the component of the magnetic force yields

$$p = qBr, \tag{2.9}$$

where relativity is ignored because the scattered proton energies were sufficiently low (usually around 50 MeV to 100 MeV). Since the proton's charge and the strength of the magnetic field were known, all that remained to calculate the proton's momentum was the radius of the circular path it traveled in the magnetic field. This could be found using the tangent lines of the proton's path found with the wire chambers before and after the magnetic field. Alternatively, the angle of deflection θ could be used to determine the proton's energy. With this angle, the proton's momentum would be calculated using the following formula:

$$p = \frac{qBl}{\sin\theta}, \tag{2.10}$$

where l is the length of the magnetic field and θ is the angle between the magnet's face and the incoming proton's path taken in the x-direction. Rather than needing the radius of curvature, which

is more complicated to determine with the tangential tracks, the angle of deflection is all that is required. However, this required precise tracking resolution, which was not possible with odd-even amplifiers not working.

2.5.4 P1 and P2 Rear Scintillators

The protons were finally detected in one of the rearmost plastic scintillators. The energy of the detected proton could be calculated using the path deflection in the magnetic field, but this relied on very accurate measurements of the proton's path before and after deflection. Since the wire chamber odd-even amplifiers did not work well, the wire chamber position could not always be ascertained to the degree of accuracy required, making this method of proton energy calculation highly inaccurate or even impossible. This is because the magnets were not very strong and did not deflect the proton very much. If the magnets were stronger, the proton's position would not need to be known to the same degree of accuracy because slight differences in proton momentum would correspond to larger path deflections.

The proton energy was instead calculated using the time of flight difference from the ΔE scintillator and the final P1 or P2 detectors, since the distance between the scintillators was known.

2.6 Neutron Detectors

The scattered neutrons were detected by a bank of nine plastic scintillators located to the left of the neutron beam. The geometry of these bars can be seen in Table 2.3. These 2-m long scintillator bars with 10-cm square cross sections were arranged vertically in a wall with phototubes at both ends of each bar. Since neutrons are not charged, they can only be detected when they collide with a proton in the detector. Since the recoiling proton is charged, it will excite the molecules in the plastic and the subsequent photons released after the molecules de-excite are detected by the photomultiplier tubes at either end of the detector. There is no way to determine whether a particle detected in the scintillator is a scattered proton or a proton knocked by a scattered neutron. The only way this can be determined is if the particle detected in the neutron bar is detected in coincidence with a proton

in the magnetic spectrometer; since a deuteron only has one proton the other particle detected at the conjugate angle is assumed to be a neutron. Accidental coincidences from background would be subtracted from the data in determining final cross sections by subtracting the background found with empty target runs.

Table 2.3 Geometry of the neutron detector array.

	Distance from Target*		Angle between Detector Edge and Beam	
	Beam side (cm)	Outside (cm)	Beam side (°)	Outside (°)
NB1	253	253	56	57
NB2	253	251	57	60
NB3	251	250	60	62
NB4	250	249	62	64
NB5	249	248	64	67
NB6	248	249	67	69
NB7	249	249	69	71
NB8	249	250	71	74
NB9	250	251	74	76

*Distance from center of target to top of front face of detector.

Figure 2.15 shows the position of two thin horizontally-oriented plastic scintillators, which were used for height calibration of events along the neutron bars. To determine the height of an event, each vertical bar was equipped with a PMT at each end. In this way, a particle interacting with the neutron detector set off two signals, one at the top and one at the bottom of the neutron bar. The time difference between the two signals made it possible to pinpoint the vertical position of the hit, explained more fully in Section 3.2.3.1.

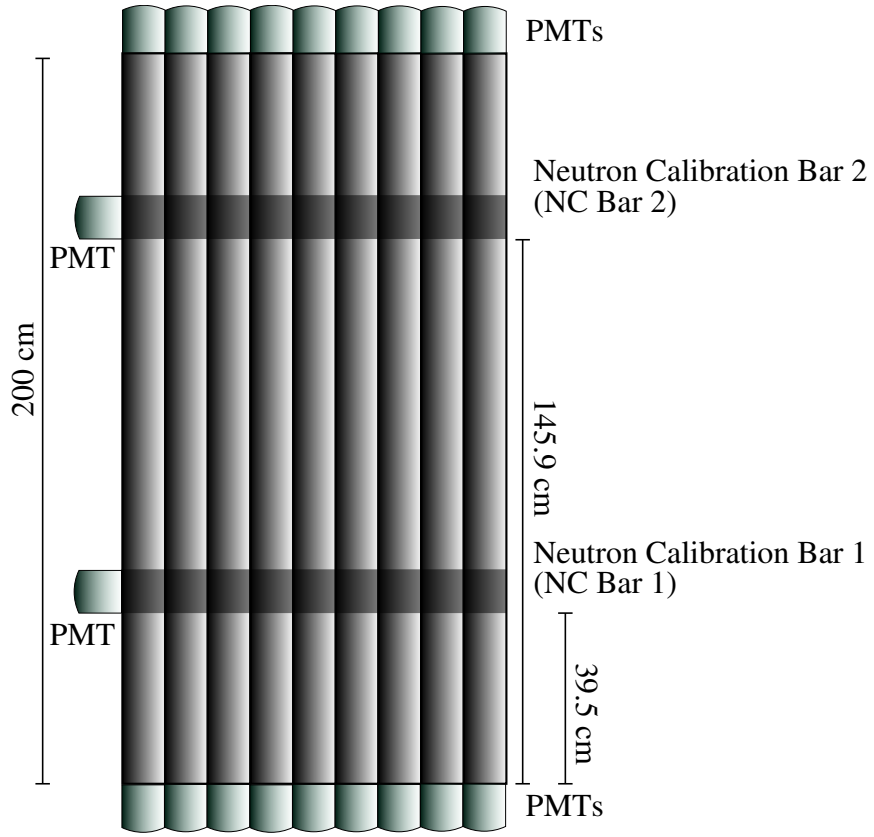

Figure 2.15 Front view schematic of the neutron detectors. The array of 2-m tall plastic scintillators was used to detect scattered neutrons. The time difference between the top and the bottom PMT determined the height of the event, calibrated using the neutron calibration bars.

2.7 Elastic Monitor

To normalize the data collected from the $n-d$ breakup experiment, an "elastic monitor" detector was used, which consisted of a thin plastic ΔE2 detector and an inorganic CsI scintillator. The 2.5-mm thick ΔE2 detector and the 14-cm thick CsI detector both had 9.6-cm square faces. This detector was at 40° to beam left to detect elastically scattered deuterons. Because the pulse height from a particle passing through each detector was proportional the energy lost in the detector, the pulse height from the ΔE2 detector plotted against the pulse height from the CsI detector could be used for particle identification, since the relationship depends on the the particle's mass and

height. The final count of elastically scattered deuterons could be used to normalize the number of scattering centers in the target.

2.8 Electronics and Data Acquisition

2.8.1 Detector Circuitry

The electronics circuit for the breakup experiment recorded the pulse height and time for each detector, sorted out the events using a logic trigger circuit, and counted total events using scalers.

The electronic circuit for each neutron detector is seen in Figure 2.16. In this circuit, the pulse height from both top and bottom PMTs was gated and read into the FERA ADC to be recorded. The time of the pulse was also recorded by the FERA TDC. The mean time of the coincidence of the pulses from the top and bottom PMT was used to determine the event trigger. The number of events from both detectors was counted by a scaler as was the number of coincidences.

The proton detector circuit was similar with slightly different logic requirements—the ΔE1 required to be in coincidence with either the P1 or P2 detectors (see Figure 2.17). The elastic detector also worked similarly with ΔE2 in coincidence with the CsI detector as seen in Figure 2.18. The fission chamber information was read in on a separate CAMAC (Computer Automated Measurement and Control) module as were the scalers.

2.8.2 Trigger Logic

The trigger logic circuit sorted events by different trigger types shown in Figure 2.19. These types were (1) proton singles, where a proton was detected in the magnetic spectrometer, determined by P1 or P2 in coincidence with ΔE1; (2) neutron singles, where a "neutron" was detected in a neutron bar; (3) NP coincidences, where a neutron was detected in a neutron bar in coincidence with a proton in the proton arm; (4) cosmic events, where at least four neutron bars detected a particle within a short time interval, presumably from a cosmic ray traversing the detectors; and (5) elastic events, where a particle was detected in the elastic monitor, determined by a coincidence of the ΔE2 detector and CsI detector. The latter two triggers were used to calibrate neutron detectors and

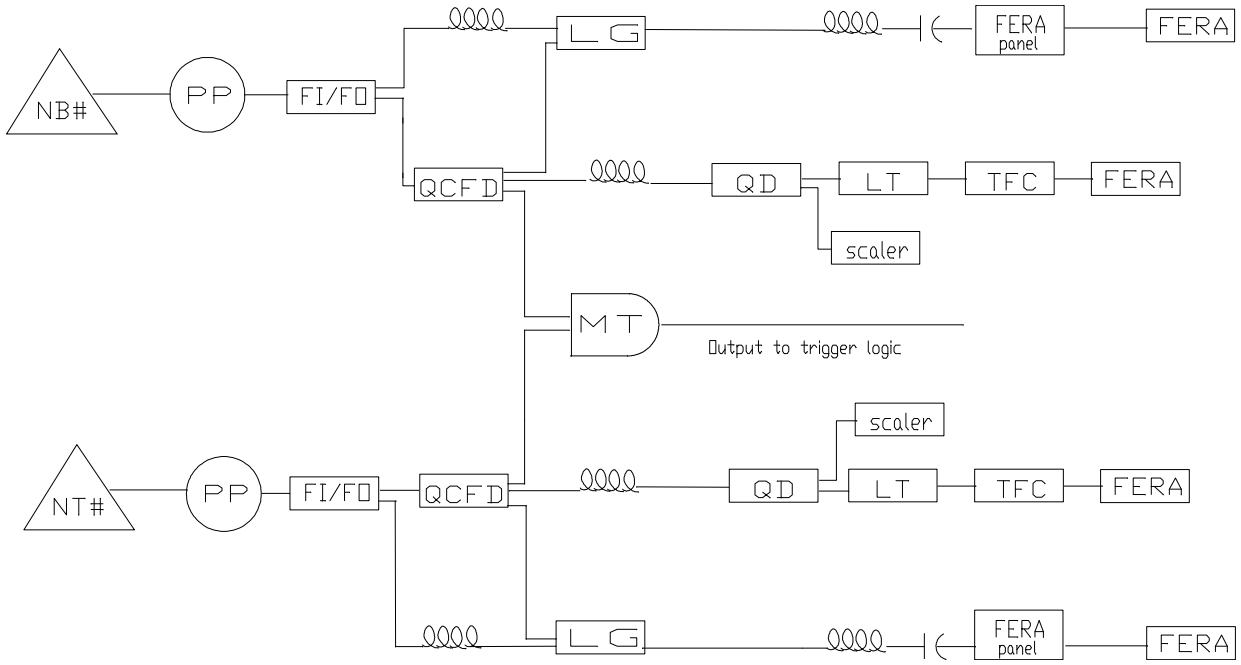

Figure 2.16 Electronic diagram for a neutron detector. The pulses from the detector's top and bottom PMTs were recorded by ADC and TDC FERA modules. The coincidence was used to create a trigger for a neutron detection.

normalize the data collected, respectively. Each of these triggers was read into a TDC FERA, so software cuts could be made using each of the triggers.

2.8.3 The Data Acquisition System

All the FERA modules had a common start coming from the event trigger. The stop for each channel on the modules came from the individual detectors. The T_0 pulse, used to stop the T_0 TDC, came from the proton pick-off right before the proton beam hit the tungsten spallation target at Target 4. Subtracting the T_0 TDC from each detector's TDC spectrum yielded the TOF (in channels).

The CAMAC modules were read out between macropulses by a computer running the MIDAS (Maximum Integration Data Acquisition System) frontend. The data was then written to files in MIDAS format. These files were read by the online analyzer and were later converted to text files

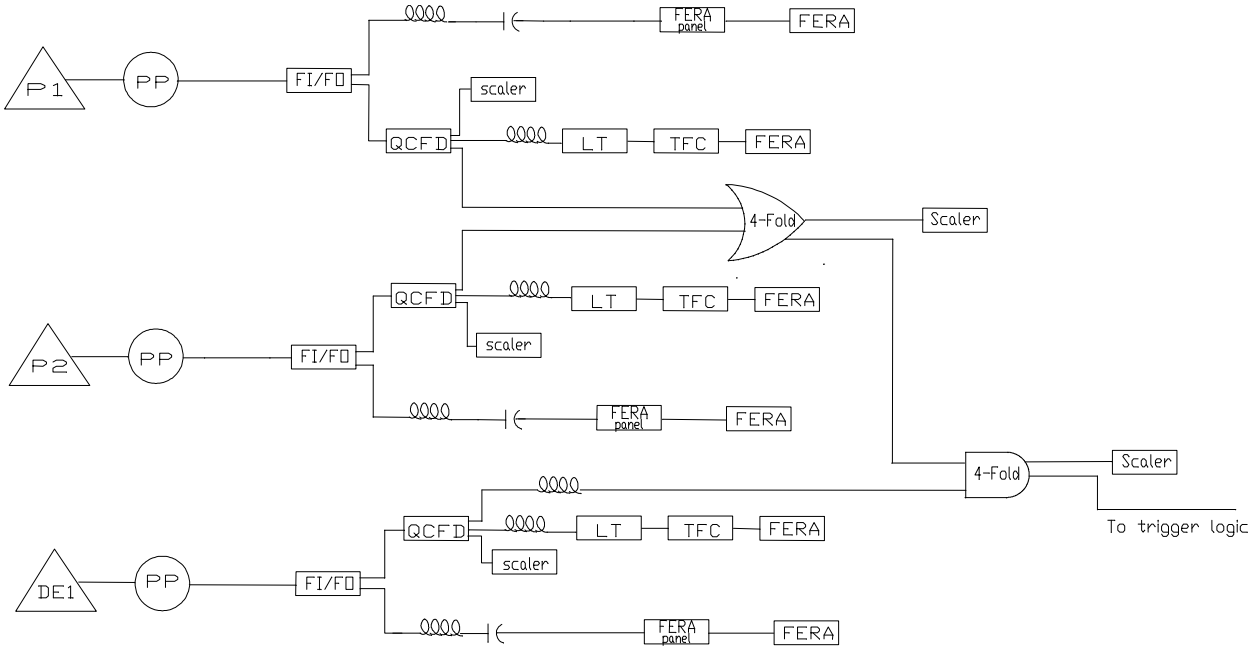

Figure 2.17 Electronic diagram for proton detectors. The pulses from the ΔE1 and P1 and P2 PMTs were recorded by ADC and FERA modules. The ΔE1 in coincidence with either the P1 or P2 detectors was used to create a trigger for proton singles events.

to be turned into ROOT trees for offline analysis. The online analyzer was written using MIDAS, C++, and ROOT libraries and histogrammed events. Offline analysis was conducted using ROOT C++ scripts.

Scalers were used to monitor the deadtime for the system. There were two sources of deadtime: electronic deadtime and computer deadtime. Electronic deadtime ocurred when the electronics were too busy processing pulses to accept more pulses. The width of the master trigger (290 ns) "blanked out" the electronics and was long enough to make the electronic deadtime uniform for all detectors. Computer deadtime occured when the acquisition system was reading in data and unable to receive data. Using scalers, which have essentially no deadtime, it was possible to determine the deadtime by comparing the scaler values to the recorded events. This assumes events analyzed had the same distribution as events lost to deadtime or overflows.

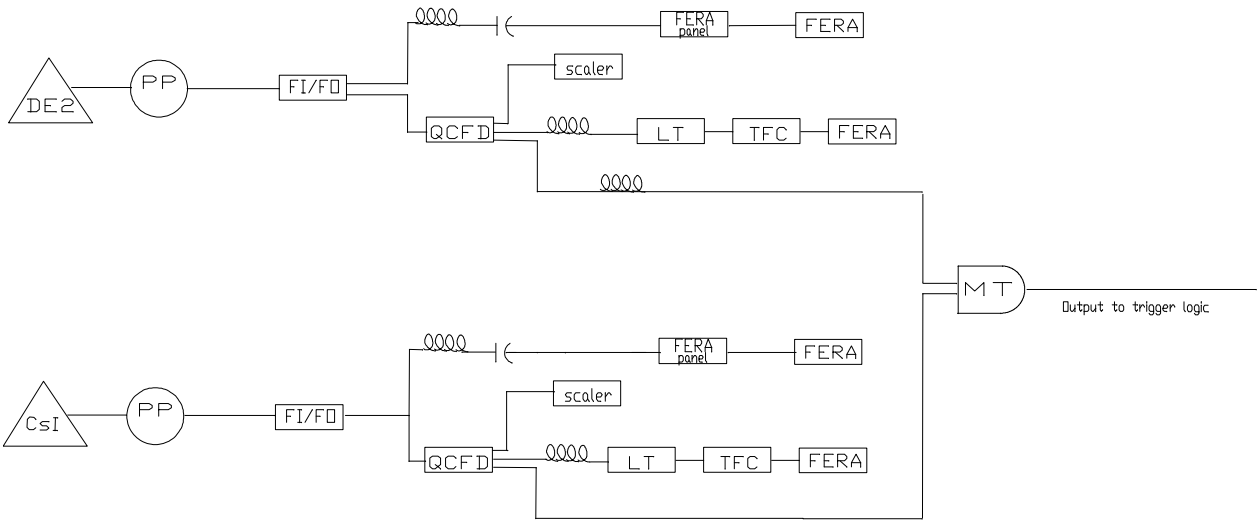

Figure 2.18 Electronic diagram for elastic spectrometer. The pulses from the ΔE2 and CsI PMTs were recorded by ADC and TDC FERA modules. The coincidence was used to create a trigger for elastic scattering events.

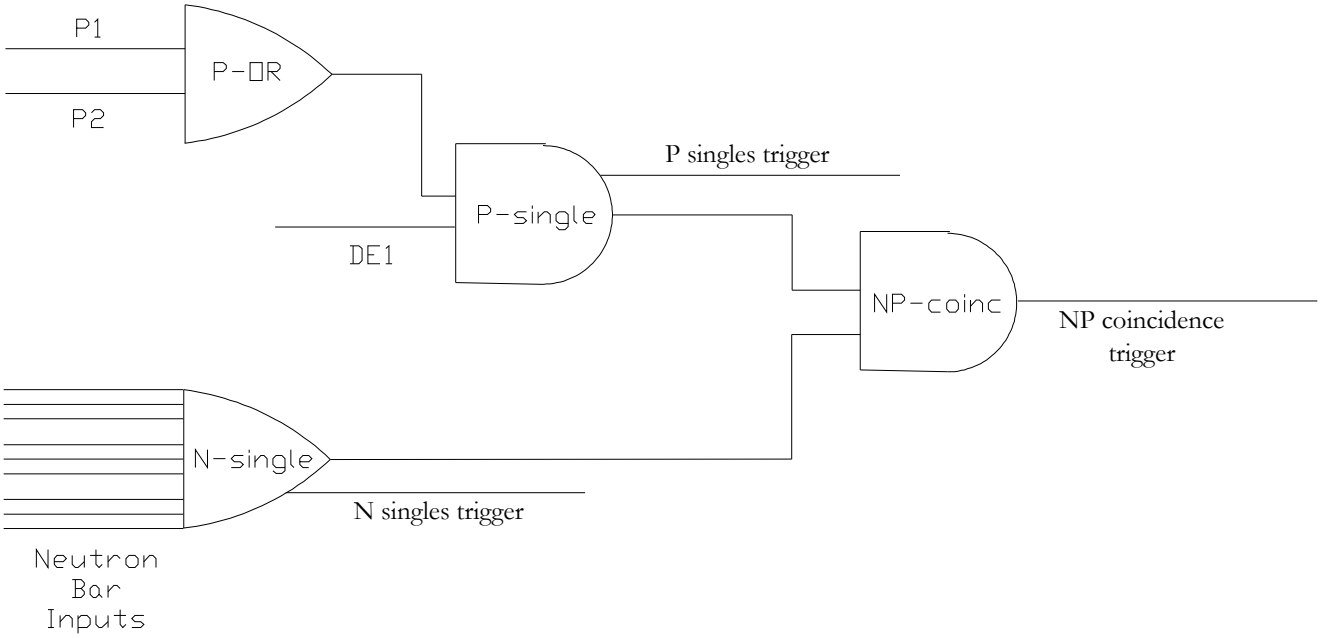

Figure 2.19 Simplified trigger logic circuit. A coincidence of a rear proton scintillator with the ΔE1 formed a P-singles trigger, indicating a proton traveled through the magnetic spectrometer. The P-singles trigger in coincidence with a N-singles trigger, from a neutron detected in a neutron bar, formed an N-P coincidence trigger, which indicated a deuteron breakup event.

Chapter 3

ANALYSIS

3.1 Cross Section Formula

The purpose of the experiment was to measure the cross section for the $d(n,np)n$ reaction. There were several parameters that had to be calculated in order to find the differential cross section:

$$\frac{d^5\sigma(\theta_n,\theta_p,E_n,E_p,E_{inc})}{d\Omega_n d\Omega_p dE_n dE_p dE_{inc}} = \frac{N_d \varepsilon_n \varepsilon_p f_l}{N_{inc} N_t \Delta\Omega_n \Delta\Omega_p \Delta E_n \Delta E_p \Delta E_{inc}}, \tag{3.1}$$

where

N_d is the number of detected proton-neutron coincidences,

N_{inc} is the number of incident neutrons,

N_t is the number of scattering centers,

$\Delta\Omega_n$ is the solid angle acceptance for scattered neutrons,

$\Delta\Omega_p$ is the solid angle acceptance for scattered protons,

ΔE_n is the range of outgoing neutron energy,

ΔE_p is the range of outgoing proton energy,

ΔE_{inc} is the range of incident neutron energy,

ε_n is the neutron detection efficiency,

ε_p is the proton detection efficiency, and

f_l is the deadtime correction.

In order to determine the cross section, each one of these quantities had to be known. The following sections describe the process used to find these quantities.

3.2 Energy Calculations

3.2.1 Time Calibration

To find the differential cross sections, it was necessary to calculate the energies of the incident and outgoing particles. This information was used to sort events by incident energy and scattered

energies for protons and neutrons, so the cross section could be given as a function of incident and scattered energies. The energies were calculated using time of flight, with the time information retrieved from the TDC spectra.

Since the FERA TDCs output time information in channels, the channel-time relationship had to be calculated. This time calibration was done using two methods. The primary method involved running the outputs of a time calibrator through the Level Translators. The time calibrator emitted pulses at set intervals; in this case, a 10 ns interval was chosen, so every 10 ns the time-to-FERAs received a pulse as seen in Figure 3.1. By dividing the 10 ns interval by the number of channels between each peak, which corresponded to a pulse from the time calibrator, the FERA channel could be related to time, assuming a linear relationship. This calibration was done once for the runs used in the analysis. Because the stop for the TDC timers was individual to each detector, the offset for time calibration had to be determined individually.

After determining the channel-to-time relationship, the times were still meaningless without knowing what they were in relationship to. This offset could be determined by subtracting T_0 TDC (in nsec) from the TDC spectrum (in nsec) of each detector. This results in a spectrum with a sharp, separate peak on the left side of the spectrum. This sharp peak is a gamma flash, a burst of photons from the proton beam impinging on the tungsten spallation target. Since the beam path length (L_0) from the spallation target to the deuterium target and the distance from the deuterium target to the detectors is known, the entire path length travelled by the gamma flash could be divided by the speed of light to yield the exact time the gamma flash arrived.

At one point during the experiment, the TFC calibration changed. This was noticed when a FERA spike[1] drifted on two of the modules (modules 6 and 8). As a result, the TFC calibration method was changed to accommodate any subsequent drifting of the TDCs that might occur. As can be seen in Figure 3.2, each TDC FERA had two inputs added. These inputs were delayed copies (40.6 ns and 165.5 ns respectively) of the gate which started the TDC FERA modules. Since the amount of delay was known and each input of a given FERA module had nearly the same TFC calibration constants, the two peaks resulting from these inputs were used from then on

[1]This spike was assumed to be a property of the FERA, since all the detectors in that module had this feature.

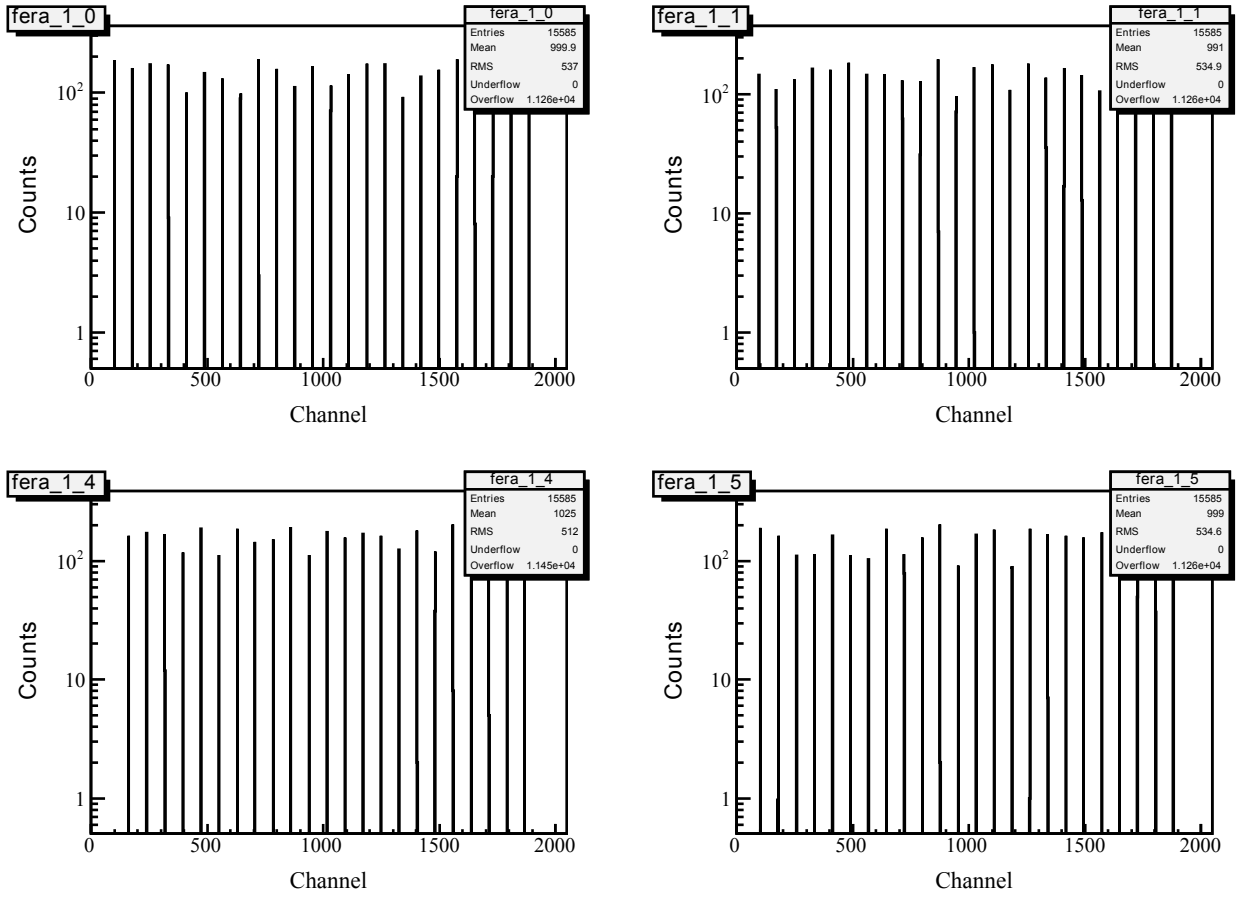

Figure 3.1 Time calibrator TDC spectra. The raw FERA output of four channels from a single FERA module are shown above. Each peak is separated by 10ns, pre-set on the time calibrator.

to automatically recalibrate the TDCs for each event.

3.2.2 Scattered Proton Energy

3.2.2.1 Wire Fitting

To find the scattered proton energy using the magnetic spectrometer, the trajectory of the scattered proton had to be ascertained using wire chamber tracking. This relied on a correctly calibrated wire chamber, which involves finding the absolute position of the anode wire which collected the

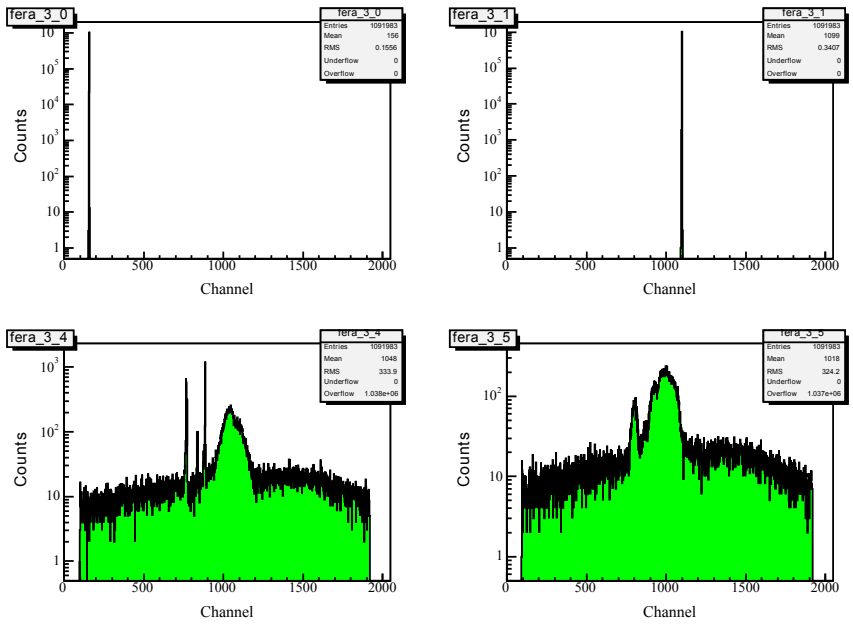

Figure 3.2 FERA TFC calibration peaks. A delayed gate was sent to the first two inputs on each FERA to fine tune time calibration.

signal, the drift distance of the particle in the chamber, and on which side of the anode wire the drift distance was.

The time of the pulses from either end of the anode wires were subtracted to create a difference spectrum as seen in Figure 3.3. To find the wire positions, the maximum peak was assumed to be a wire. Then, each search for peaks was carried out to the left and right on the time difference spectrum from this channel. For a bin to be considered a peak corresponding to an anode wire, it was required to have counts greater than any bin immediately to its left or right and at least $1/8$ as many counts as the previous peak. In this way, the wire positions were determined. This information from the anode wires only gives the proton's path to within 8.125 mm, making it inadequate for proton trajectory reconstruction. Because the "odd-even" amplifiers needed to get better resolution were not working (see Sec. 2.5), the proton energy could not be calculated using proton path deflection. Subsequent analysis reveals the wire fitting as adequate resolution for "binning" the cross section by proton scattering angle, with the proton energy coming from TOF.

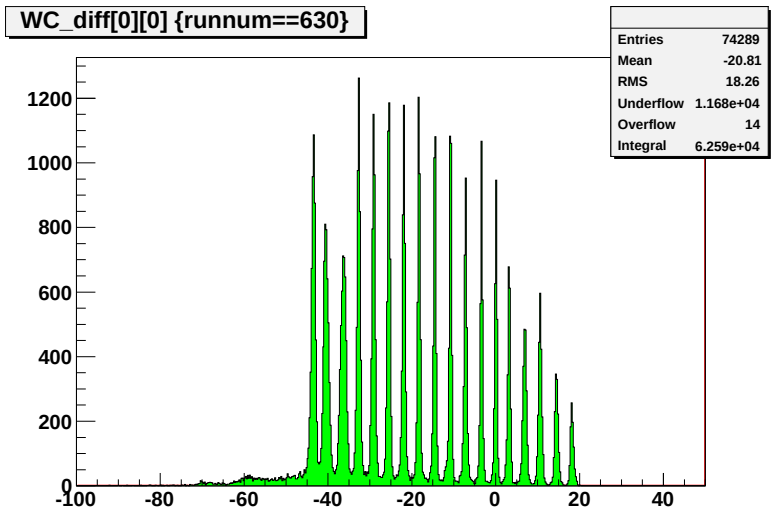

Figure 3.3 Wire chamber time difference spectrum. The time difference in nanoseconds from the anode wires on the first *x*-plane of wire chamber 1.

3.2.2.2 Wire to Wire Calibrations

Using data collected with a polyethylene target and magnets lowered, the absolute position of the wires was found by cutting the time difference spectra for each *x* plane on the finger detectors, small position calibration detectors placed at the rear of the magnetic spectrometer. This can be seen in Figure 3.4, where a proton from the target detected by a finger would be correlated to a small group of adjacent wire numbers. From these cuts, the associated wire number could be determined for each plane. Table 3.1 shows the wire number corresponding to the center of a cut on the fingers for each *x*-plane. The fingers were clearly correlated to the wire number in the rear wire chambers, but not in the front wire chambers, due to the non-pointlike target. These values can be compared to the wire to wire calibrations explained later.

Similarly, to get wire to wire correlations, the wire numbers in the second *x*-plane of wire chamber 4 were compared to the wire numbers in the other x-planes. Cutting the time difference spectra for each *x* plane on a wire number from the final *x*-plane yielded the plot seen in Figure 3.5.

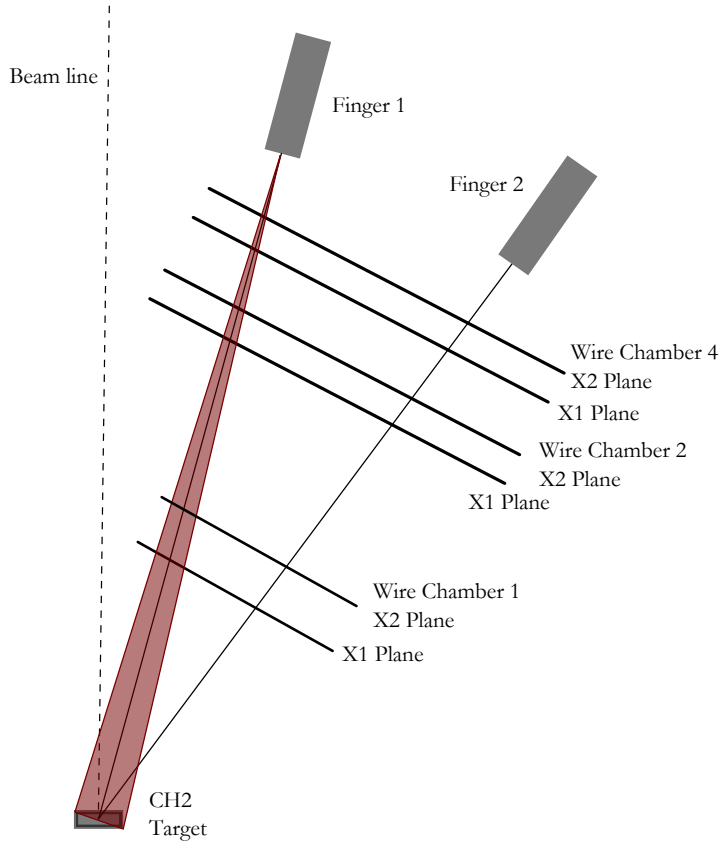

Figure 3.4 Finger detectors and wire to wire correlation. Not to scale. The black line passing from the target to the Finger 2 shows that there should be a correlation between wire numbers in each plane for events coming from the target detected by a finger detector. The target shape causes a spread to appear in the first couple wire planes when cutting on the finger detectors.

The associated wire number from the second x-plane in wire chamber 4 for each finger is shaded in on Figs. 3.5 and 3.6. It can be seen that the wire numbers on the rear planes were well correlated with the final x-plane, but the front planes do not have a good correlation.

The distributions of the peaks from cutting on the wire numbers for the front planes were more spread out as expected from a non-pointlike target (see Figure 3.4), but the flat section of the plot for WC1 planes was unexpected. Notice the linear relationship until around wire number 25. At this point, the plot plateaued. This was likely because the wires in WC4 were "out of range" of

Table 3.1 Finger cuts correlated to wire number

Plane	**Wire No. with cut on Finger 1**	**Wire No. with cut on Finger 2**
WC1X1*	15	11
WC1X2*	15	12
WC2X1	51	30
WC2X2	24	-6
WC4X1	**	18
WC4X2	60	26

Cuts for each finger detector on the wire number spectra of the *x*-planes for the wire chambers yield a wire number for the finger, which can be used to determine the absolute position of the planes.

* Spectra were unclear.

** Unable to determine.

WC1. The edge of the active region for WC1 was somewhere around this wire number. Finger 1 was then clearly out of range of WC1 and Finger 2 was borderline. Because of this, it would not be easy to calibrate the absolute angles using wires from WC1. This is important because binning events by proton scattering angle would have to be done by one of the front wire chamber planes because the magnets were left up during beamtime, making angles from the rear wire chamber planes unusable. To get around this, the absolute positions of the wires from the rear planes would have to be determined using the fingers and then these wires would have to in turn be used to calibrate the absolute positions of the wires in the front planes, rather than using the fingers to directly determine the position of the wires in the front planes. The linear relationship of the wires seen in Figure 3.6 before the plot plateaued indicates that that this is possible.

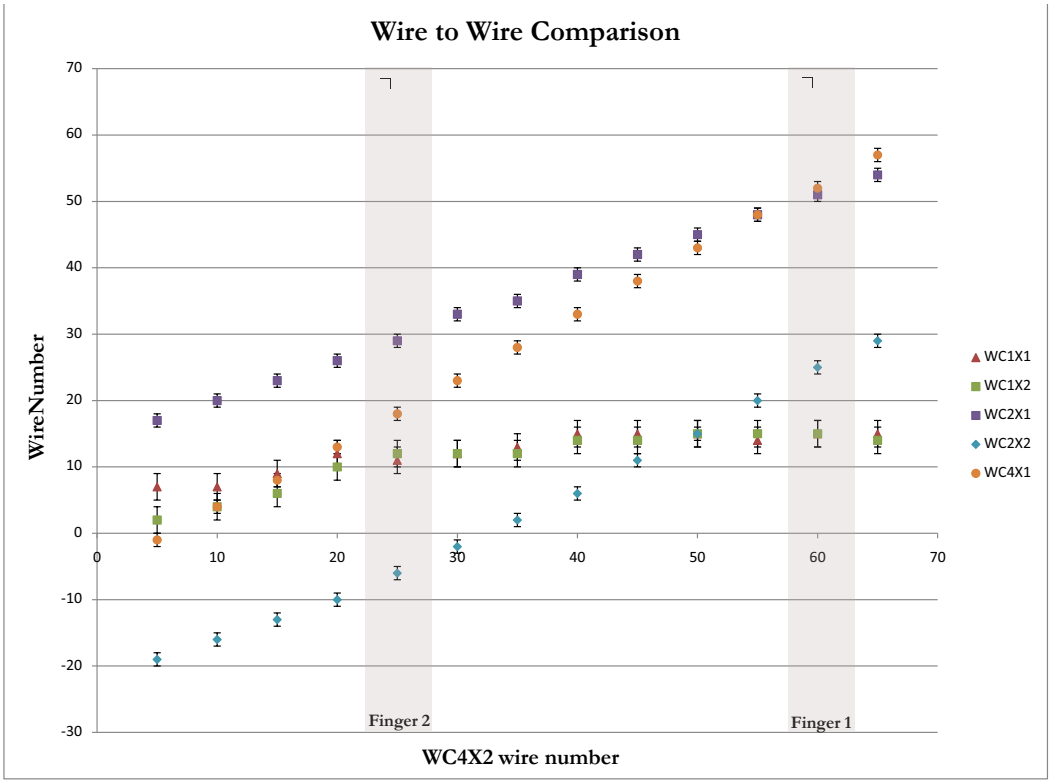

Figure 3.5 Wire to wire calibration. For each x-plane, the wire numbers of each x-plane were compared to the wire numbers in the second x-plane of wire chamber 4, by cutting the wire number spectra for each x-plane on a wire number from wire chamber 4. The wire to wire relationship was linear for the rear x-planes, but the x-planes in wire chamber 1 are not well correlated. This is not surprising due to the distance between the first and last wire chamber. The error bars indicate the width of the peak from the full-width half max.

3.2.2.3 Angular Resolution

Because the "odd-even" amplifiers did not work well, it was not possible to determine on which side of the wires the drift distance should have been added. Therefore, it was instructive to look at the angular resolution of using only the wire number information. Looking at wire chamber 1, the angular uncertainty from "binning" events by closest anode wire was approximately 4.65°. This was determined from Figure 3.7. Consider a proton travelling through and detected by a wire in

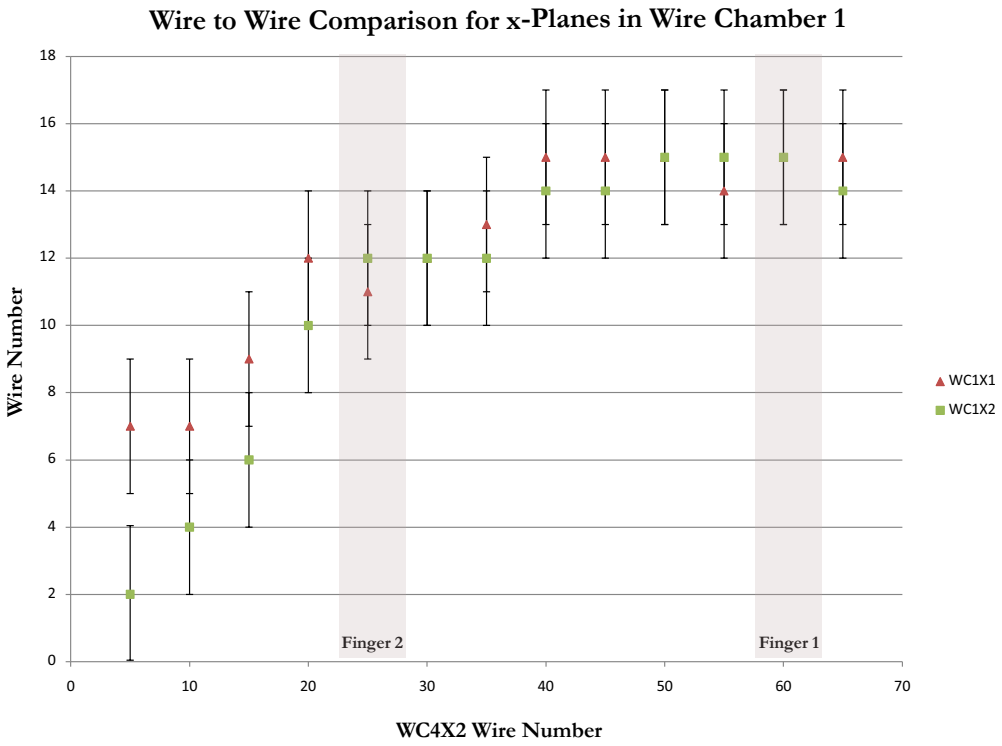

Figure 3.6 Wire to wire calibration with wire chamber 1 from Figure 3.5. Notice the linear relationship until around wire number 25. At this point, the plot plateaued. This was likely because the wires in WC4 were "out of range" of WC1. The edge of WC1 was somewhere around this wire number. Finger 1 is then clearly out of range of WC1 and Finger 2 is borderline. Because of this, it would not be easy to calibrate the absolute angles using wires from WC1.

the WC1X1 plane, and then travelling through WC1X2 plane. To determine the angular resolution, the proton could have passed through at any point between the wires, so a wire-spacing width of 0.8125 cm is assumed as the variation. If the proton's path happens to be perpendicular to the wire chamber, the angular spread is

$$\Delta\theta = \tan^{-1}\left(\frac{d}{k}\right), \tag{3.2}$$

where d is the wire-spacing width and k is the distance between the two planes. This yields an approximate angular spread of 4.65°. If the path of the proton is along the inside edge of the wire

detector, such that the path is 11.98° degrees off of the perpendicular, $\Delta\theta_1$ can be found using the law of sines:

$$\Delta\theta_1 = \sin^{-1}\left(\frac{d\sin\gamma}{l'}\right), \tag{3.3}$$

where l' can be found using the law of cosines:

$$l' = \sqrt{l^2 + d^2 + 2ld\cos\gamma}. \tag{3.4}$$

Then, $l = \dfrac{k}{\cos(11.98^\circ)}$ yielding $\Delta\theta_1 = 3.68^\circ$. Similarly, $\Delta\theta_2 = 3.73^\circ$. Thus, if the cross section is binned by angle with bins larger than 5°, it makes no sense to get a sharper resolution (by using odd-even amplifiers) than that provided by merely using the wire information from events.

Since the target is not pointlike, the path is not determined by using a single wire in a wire plane. Thus, it is necessary to account for the target's extended shape. The 1.27 cm thick target is illuminated by a 1.5-in diameter beam spot, yielding a maximum cross section of the target as 4.02 cm as seen in Figure 3.8. Given a point on the first wire chamber an average distance of l=64 cm, the possible range of angles for a given scattering angles varied by 3.6°. Again, this could be considered negligible with large enough bins for the differential cross section.

3.2.2.4 Time of Flight for Proton Energy

Instead of using the magnetic spectrometer, the velocity of the protons was calculated using the ΔE-E telescope, since the times the proton was detected in the ΔE detector and the P1 or P2 detector were known. The resolution from the drift chambers was not sufficient to determine the path of the scattered proton to use for energy analysis.

Using LISE ++ [41], a simulation program to determine transmission of particles and various other parameters including material thicknesses for spectrometers, the least amount of energy the proton could have to make it through the magnetic spectrometer was 25.7 MeV if the event occurred at the back of the target and 23.5 MeV if the event occurred at the front of the target. This energy value comes from energy loss as the proton travels through various materials in the scintillator. The criterion for making it through the magnetic spectrometer was that the proton just barely made it to the P1 or P2 rear scintillator. The materials used to calculate this included the

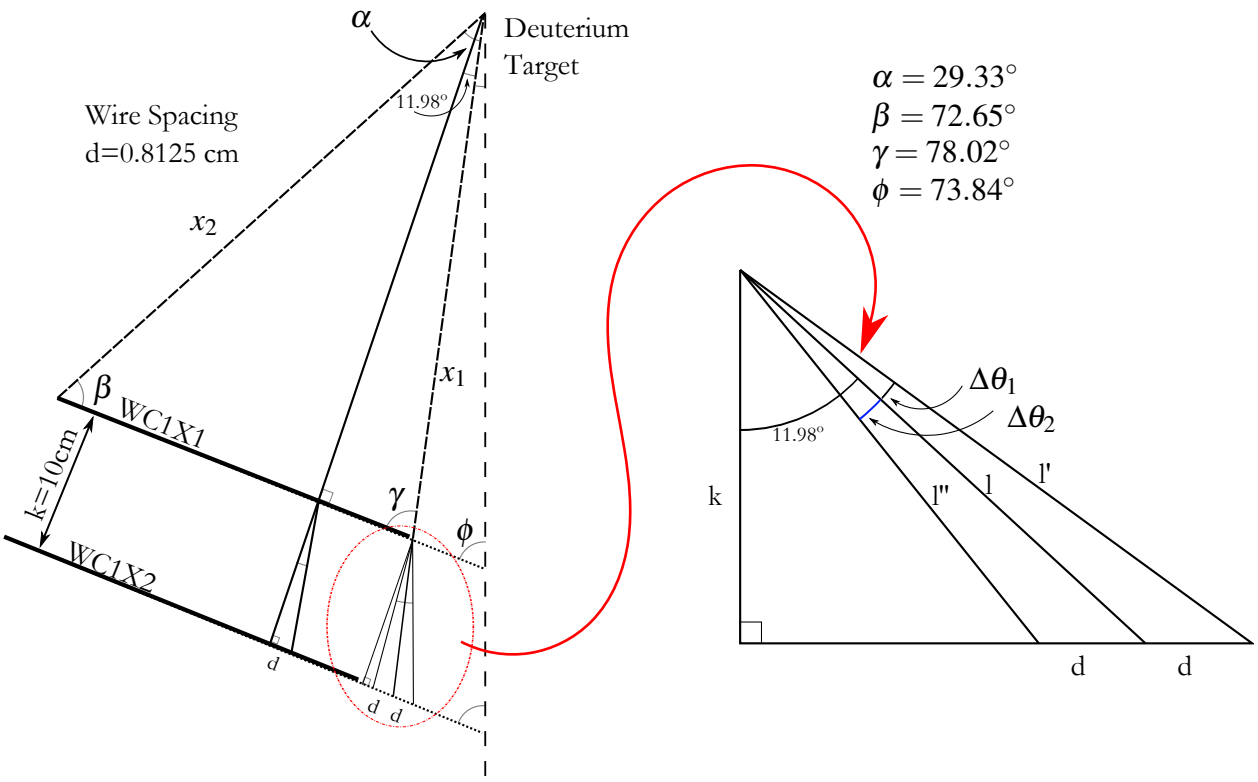

Figure 3.7 Angular resolution using wires in Wire Chamber 1. Two paths are drawn from the target to the first wire chamber planes. In each case, the uncertainty in the second plane is the width of the wire-spacing. Using this width, the angular uncertainty of the path can be determined. The greatest angular spread is a path along the perpendicular from the target to the wire chamber, yielding a spread of 4.65°. On a path along the outside edge of the wire chamber, the angular spread is under 4°. Not to scale.

mylar window of the target (50.8 μm), the kapton window of the vacuum chamber (127 μm), the scintillator material for ΔE1 and P1 or P2 (2.5 mm each), the mylar foils in each of the wire chambers (each wire chamber has a front and a rear foil that is 51 μm thick. Wire chamber 1 has eight 6.3 μm thick foils and wire chambers 2 and 4 both have seven 6.3 μm thick foils within them [42]), the isobutane-argon gas (wire chamber 1 has a 12.7 cm drift space, whereas wire chambers 2 and 4 have only 5 cm of drift space), and the air (assumed to be approximately 170 cm). With this information, LISE++ was used to calculate the minimum proton energy. Thus, scattered protons had to

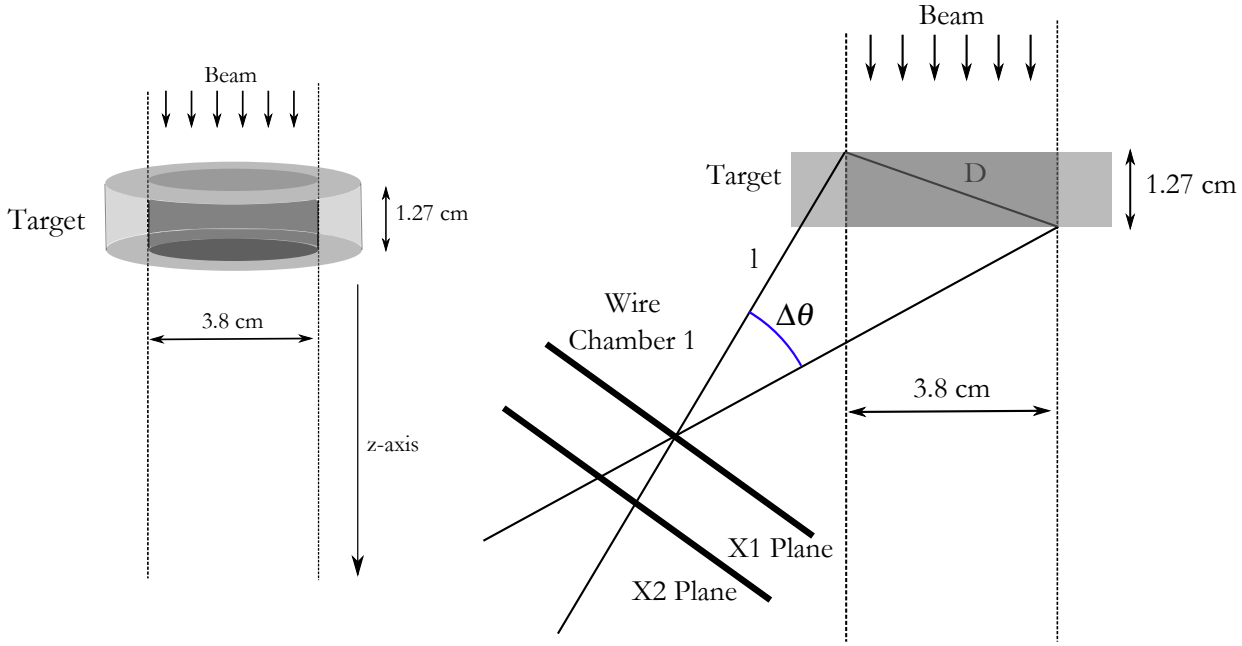

Figure 3.8 Angular resolution with extended target. On the left, the beam illuminated a 3.8 cm radius circle on the cylindrical target. Taking a slice along the z-axis, the cross section of the target is used to find the angular resolution at left. Given an average distance from the target of $l = 64$ cm, the angular distribution from the extended target is 3.6°. The target is 1.27 cm thick and is illuminated by a 3.8-cm diameter beam spot.

have greater than 25 MeV energy. This was useful to know what the lower bound is on real events. Also, this is important in converting the TOF to energy because energy losses in travelling through the spectrometer increase TOF. To correct for this, energy lost in the target would have to be added to the energy determined from the TOF between the ΔE1 and the rear P1 or P2 scintillators. To determine how the energy lost in the spectrometer affected the TOF would require a more in depth simulation, since the energy was not lost all at once.

3.2.3 Scattered Neutron Energy

3.2.3.1 Neutron Bar Height Calibration

The vertical position of an event along the neutron bar was important in the energy calculation for time of flight, since the distance traveled by the neutron depended on this height. This vertical position could be determined by finding the difference in times between the top and the bottom PMT on a neutron bar.

As can be seen in Figure 3.9, if the length of the vertical bar is defined as l and the distance from the top of the vertical bar to the hit as y, the distance from the bottom of the vertical bar to the hit is $l - y$.

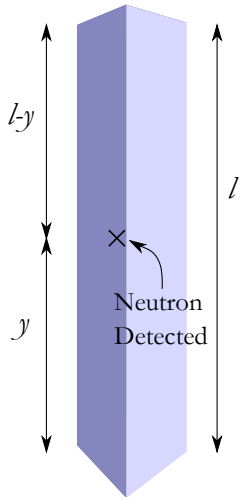

Figure 3.9 Representation of a hit on a neutron detector. The time difference between detection at the top and bottom PMTs was used to calculate the height of the event.

The time it takes for the photon to travel from the hit to the top PMT is:

$$t_t = \frac{l-y}{c} + T_{bar} + c_1, \tag{3.5}$$

where c is the speed of light in the plastic bar, T_{bar} is the TOF to the neutron bar from the target,

and c_1 is the electronic delay. Similarly, the time for the photon to travel to the bottom PMT is:

$$t_b = \frac{y}{c} + T_{bar} + c_2. \tag{3.6}$$

The difference of t_t and t_b is given with Eq. (3.7)

$$t_t - t_b = \frac{l - 2y}{c} + c_1 - c_2. \tag{3.7}$$

Solved for y, yields:

$$y = \frac{1}{2}\left(c\left(t_b - t_t + (c_1 - c_2)\right) + l\right). \tag{3.8}$$

The time difference for each neutron bar was plotted and centered around 0 as shown in Figure 3.10. To center the spectrum, offsets were added to the time from the top PMT and equal amount subtracted from the time from the bottom PMT or vice versa depending on which way the spectrum needed to be moved. In this way, the time sum was not changed. The height calibration can be seen in Figure 3.11, where the events are histogrammed by neutron bar and height.

With the height of the hit and the time it occurred known, the energy of the detected neutron could be calculated once the time the incident neutron hit the deuterium target was ascertained.

3.2.3.2 Scattered Neutron TOF Calculation

Since the proton backtracking method yields a time of event, the TOF method could be used to calculate the energy of the scattered neutron. The time when the neutron hit the neutron detector is calculated using the sum of the TOF to the top bar and the bottom bar from Eqs. (3.2.3.1) and (3.2.3.1). The time sum is

$$T_T + T_B = \frac{l}{c} + 2T_{bar} + c_1 + c_2. \tag{3.9}$$

Clearly, the time sum of the times from the top and bottom neutron detector PMTs is linearly related to the TOF to the detector (T_{bar}). Using the known distance to the neutron detectors, it is possible to set the offset by calculating where the gamma flash should appear. Then, the flight distance for the neutrons can be calculated knowing the perpendicular distance to the neutron bars and the height of the event. In this way, the TOF method can be used to find the energy of the scattered neutrons

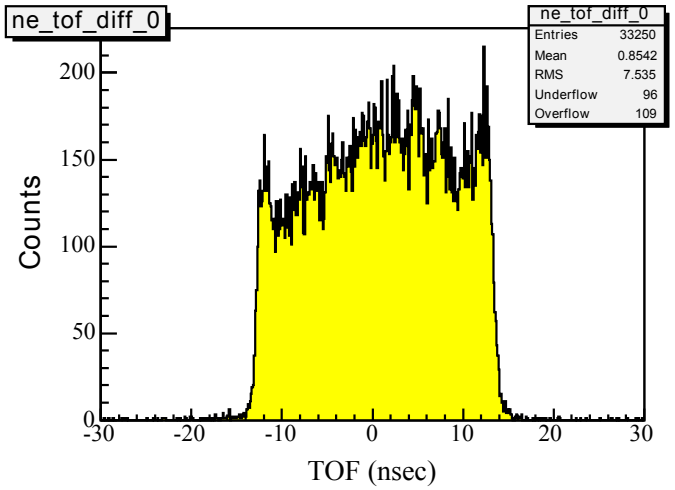

Figure 3.10 Time difference spectrum for neutron bar 1. The TOF to the top PMT subtracted from the bottom PMT yielded a spectrum in nanoseconds with a sharp drop off, clearly delineating the edge of the neutron bar. The time difference for the edges and the time difference for the horizontal neutron bars were used to calibrate the neutron height, so a given time difference yields a height along the neutron bar in centimeters relative to beam height.

3.2.4 Incident Neutron Energy

To calculate the TOF of the incident neutrons, the velocity of the protons had to be calculated first. The path of the proton could be projected back toward the deuterium target, so the TOF from the target to the ΔE detector could be calculated. Thus, the time that the incident neutron interacted with the deuteron target was known. Since the length of the incident neutron path was known to be 16.93 m and T_0 was given[2], the velocity and energy of the incident neutrons could be calculated.

3.3 Solid Angle Calculations

The solid angle could be determined for both neutron detection and proton detection using the geometry of the experimental setup. The solid angle can be found using the known measurements

[2] A T_0 pulse was delivered to experimenters at WNR whenever a proton pulse hit the spallation target.

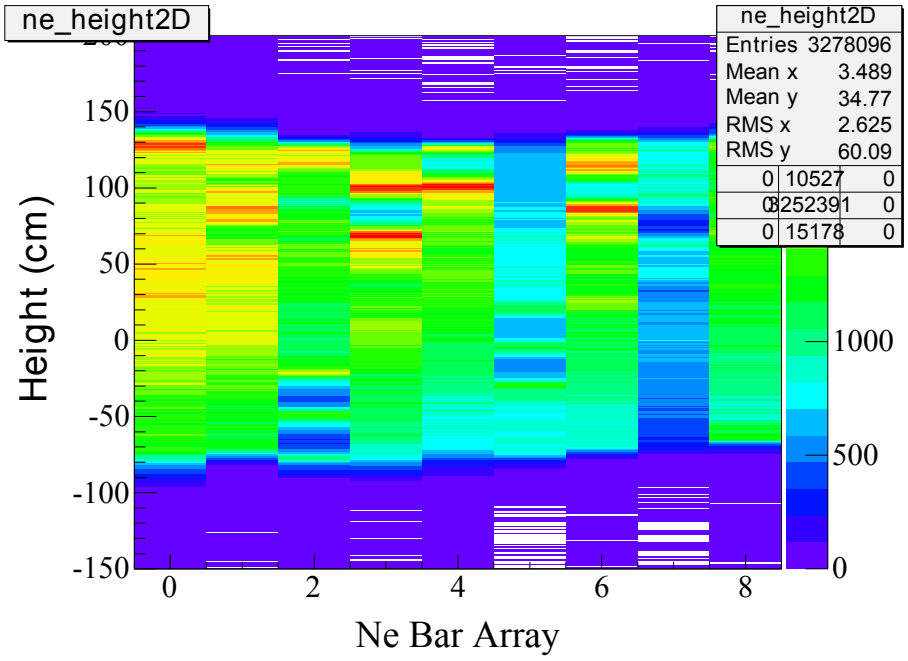

Figure 3.11 The calibrated height spectra. The TOF difference was converted to a neutron height in centimeters relative to the beam height, using the edges of the bars and the positions of the neutron calibration bars, which are seen as horizontal bands in the second spectrum. On these spectra, the x-axis is reversed, so bar 9 is 0 and bar 1 is 8 on the axis. This represents looking at the neutron array from the target, so the neutron bar closest to the beam is on the left.

of each detector, so

$$\Omega = \int \frac{dA}{r'^2} = \int_{-d}^{e} \int_{0}^{b} \frac{dxdy}{y^2 + x^2 + c^2 - 2cx\cos(u)}, \tag{3.10}$$

where c is the beamside distance to the detector, b is the detector width, $d+e$ is the detector height with e found from subtracting beam height from the height value shown in Tables 2.2 and 2.3. All needed values can come from Tables 2.1, 2.2, and 2.3

3.4 Analysis Remaining

The analysis on the data is not complete and cross sections have not yet been determined. Corrections to the number of detected events is incomplete due to lack of analysis on neutron detection

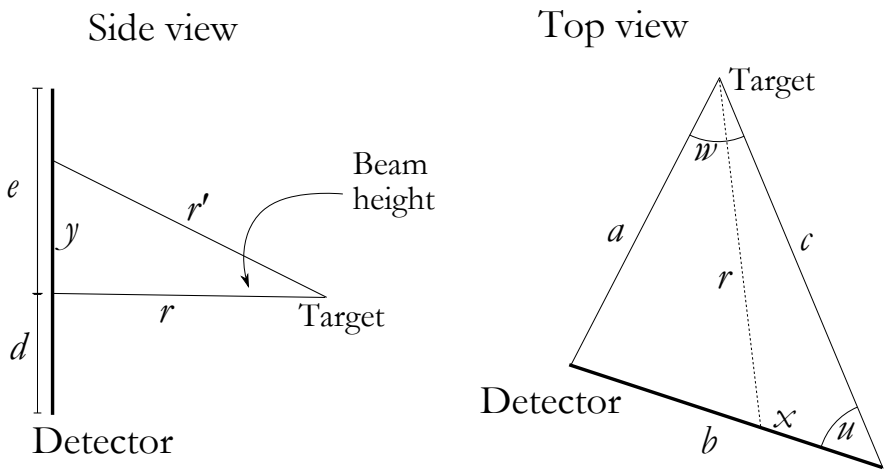

Figure 3.12 Solid angle calculations. Left is a side view of the detector with height *d*+*e*. The top view of the detector (right) shows distances *a*, *b*, and *c* for each detector, measurements found in Tables 2.1, 2.2, and 2.3. Angles *w* and *u* could be calculated from measurements of distances. From these, the solid angle for each detector could be determined.

efficiency, proton detection efficiency, and deadtime. A discussion of deadtime can be found in Section 2.8.3. A Monte Carlo simulation could be used to calculate neutron and proton detection efficiencies. Calibration of the neutron detector ADC spectra using cosmic rays would help help set ADC thresholds for use in neutron efficiency calculations. Also, these values could be obtained from $n-p$ elastic scattering from the data with a liquid hydrogen target.

The incident neutron number can be determined by analyzing the fission chamber data. This is done by determining how many fission events there are and using the neutron-induced fission cross section for ^{238}U to determine the incident neutron flux. Although preliminary analysis of this has been done by Turkewitz [43], analysis of efficiencies and deadtime for the fission chamber was not done.

The number of scattering centers can be determined by normalizing with $n-d$ elastic data from the ΔE2-CsI telescope. The deuterium target's temperature was recorded as well as the volume of liquid deuterium in the target, so the number of scattering centers could be found using stoichiometry, but this only works as an approximation due to the presence of gas bubbles in the

liquid deuterium, so instead the target thickness was left as a free parameter in the experiment and could be fixed when the $n-d$ elastic scattering data collected from the ΔE2-CsI telescope is used to normalize the data [11]. According to preliminary analysis done by [43], the physical target thickness was measured to be 2.8 cm, but results from the analysis calculated the effective thickness of the target to be approximately 1.8 times the physical thickness. This is thought to be incorrect and Turkewitz proposes there were possible errors in incident neutron flux determination.

Chapter 4

CONCLUSIONS

Analysis from the $d(n,np)n$ data collected in 2009 is not yet complete for this and while there are no immediate plans for analysis to continue, there is no reason why it should not continue. From analysis already completed, it is clear that future analysis should not attempt to find proton energy using the proton magnetic spectrometer. Using TOF would be the best recourse, using the rearmost wire plane in the first wire chamber to bin by angle.

Problems from previous analysis of this data [44] need to be addressed. One of these problems is a double band found in a histogram of scattered proton energy against incident neutron energy. There are two well-correlated bands. One could be due to $n-d$ elastic scattering, but the hydrogen data has not been analyzed to see if this band disappears. If it does not, empty target runs should also be analyzed to see if this correlation might actually be part of the background.

This series of experiments will not likely continue in the near future because the beamline this experiment used has been torn down. This flight path and others were demolished to make space for a new building enclosing multiple flight paths. Reconstruction of this flight path would be costly and funding for this has not yet been found.

BIBLIOGRAPHY

[1] R. Machleidt. *Phys. Rev. C* **63**, 024001-1 (2001).

[2] V. G. J. Stoks *et al*. *Phys. Rev. C* **49**, 2950 (1994).

[3] M. Stephan *et al*. *Phys. Rev. C* **39**, 2133 (1989).

[4] J. Kuroś-Żołnierczuk *et al*. *Phys. Rev. C* **66**, 024003 (2002).

[5] B. S. Pudliner *et al*. *Phys. Rev. C* **56**, 1720 (1997).

[6] S. A. Coon *et al*. *Nucl. Phys. A* **317**, 242 (1979).

[7] G. Igo *et al*. *Nucl. Phys. A* **195**, 33 (1972).

[8] R. E. Adelberger and C. N. Brown. *Phys. Rev. D* **5**, 2139 (1972).

[9] K. Ermisch *et al*. *Phys. Rev. C* **68**, 051001-1 (2003).

[10] H. Witala et al. *Phys. Rev. Lett.* **81** , 1183 (1998).

[11] M. B. Chtangeev. Master's thesis, Massachusetts Institute of Technology, 2005.

[12] J. Kuroś-Żołnierczuk *et al*. *Phys. Rev. C* **66**, 024004 (2002).

[13] C. Wells. Bachelor's thesis, Houghton College, 2005.

[14] J. L. Matthews *et al*. LANSCE Proposal No. 20071544. 2007 (unpublished).

[15] J. M. Laborie *et al*. *Nucl. Instrum. Methods B* **248**, 329 (2006).

[16] G. Pauletta and F. D. Brooks. *Nucl. Phys. A* **255**, 267 (1975).

[17] M. Holmberg. *Nucl. Phys. A* **129**, 327 (1969).

[18] M. B. Chadwick *et al*. *Nuclear Data Sheets* **107**, 2931 (2006).

[19] W. Pairsuwan *et al*. *Phys. Rev. C* **52**, 2552 (1995).

[20] M. Eslami-Kalantari. PhD thesis, University of Groningen, Groningen, Netherlands, 2009.

[21] D. R. Tilley, H. R. Weller, and H. H. Hasan. *Nucl. Phys. A* **474**, 1 (1987).

[22] C. R. Howell *et al*. *Phys. Rev. Lett.* **61**, 1565 (1988).

[23] J. Strate *et al*. *Nucl. Phys. A* **501**, 51 (1989).

[24] M. Allet *et al*. *Phys. Rev. C* **50**, 602 (1994).

[25] H. Shimizu *et al*. *Nucl. Phys. A* **380**, 111 (1982).

[26] St. Kistryn *et al*. *Nucl. Phys. A* **548**, 49 (1992).

[27] J. Balewski *et al*. *Nucl. Phys. A* **581**, 131 (1995).

[28] G. Rauprich *et al*. *Nucl. Phys. A* **535**, 313 (1991).

[29] J. Zejma *et al*. *Phys. Rev. C* **55**, 42 (1997).

[30] St. Kistryn *et al*. *Phys. Rev. C* **68**, 054004 (2003).

[31] St. Kistryn *et al*. *Phys. Rev. C* **72**, 044006 (2005).

[32] A. Ohlson. Bachelor's thesis, Massachusetts Institute of Technology, 2009.

[33] S. A. Wender *et al*. *Nucl. Instr. and Meth.* **336**, 226-231 (1993).

[34] M. Eriksson. Master's thesis, Royal Institute of Technology, Stockholm, 1998.

[35] K. F. Schoenberg and P. L. Lisowski. *Los Alamos Sci.* **30**, 7 (2006).

[36] M. S. Livingston and J. P. Blewett. *Particle Accelerators*. McGraw-Hill Book Company, New York, 1962.

[37] D. K. Hyer and R. Pynn. *Los Alamos Sci.* **19**, 46 (1990).

[38] LANSCE Operations. WNR status. http://lansceoperations.lanl.gov/operations/Status/WNR_Status.shtml. Accessed Aug 21, 2009.

[39] R. J. De Young. Bachelor's thesis, Houghton College, 2003.

[40] K. K. Boddy. Bachelor's thesis, Massachusetts Institute of Technology, 2007.

[41] O. B. Tarasov and D. Bazin. *Nucl. Phys. A* **746**, 411 (2004).

[42] C. L. Morris. *Nucl. Instr. and Meth.* **196**, 263 (1982).

[43] J. Turkewitz. Bachelor's thesis, Massachusetts Institute of Technology, 2010.

[44] S. Uemura. Bachelor's thesis, Massachusetts Institute of Technology, 2010.